Characterization and mapping of surface physical properties of Mars from CRISM multi-angular data: application to Gusev Crater and Meridiani Planum

J. Fernando[1,2], F. Schmidt[1,2], C. Pilorget[3], P. Pinet[4,5], X. Ceamanos[6], S. Douté[7], Y. Daydou[4,5], F. Costard[1,2]

[1]Univ. Paris-Sud, GEOPS, UMR 8148, Orsay, 91405, France [2]CNRS, Orsay, 91405, France, jennifer.fernando@u-psud.fr [3]Division of Geological and Planetary Sciences, Caltech, Pasadena, California, USA [4]Univ. de Toulouse, UPS-OMP, Toulouse, France [5]CNRS, IRAP, Toulouse, France [6]Météo France/CNRS, CNRM/GAME, Toulouse, France, [7]Univ. Joseph Fourier/CNRS, IPAG, Grenoble, France

arXiv:1408.5301v2 [astro-ph.EP] 21 Mar 2015

Abstract

The analysis of particle physical properties (grain size, shape and internal structure) and its organization (surface porosity, roughness, and grain size distribution) provides information about the geological processes which formed and modified planetary surfaces. CRISM (Compact Reconnaissance Imaging Spectrometer for Mars) multi-angular observations (varied emission angles) allow for the characterization of the surface scattering behavior, which depends on the composition and on the material physical properties such as the grain size, shape, internal structure, and the surface roughness. After an atmospheric correction (compensating mineral aerosol effects) by the Multi-angle Approach for Retrieval of the Surface Reflectance from CRISM Observations (MARS-ReCO), the surface reflectances at different geometries were analyzed by inverting the Hapke photometric model depending on six parameters: single scattering albedo, 2 phase function terms, macroscopic roughness and 2 opposition effects terms. In this work, surface photometric maps are created to observe the spatial variations of surface scattering properties as a function of geological units. Information regarding the single scattering albedo, the particle phase function and the macroscopic roughness are provided at the CRISM spatial resolution (200m/pixel). This article describes the application of this methodology to the data covering the Mars Exploration Rover (MER) landing sites located at Gusev Crater and Meridiani Planum where orbital and in situ observations are available. Complementary orbital observations (e.g., CRISM spectra, THermal EMission Imaging System (THEMIS), High Resolution Imaging Science Experiment, (HiRISE) images) were used for interpreting the modeled Hapke photometric parameters in terms of physical properties which can be used to constrain the geological processes. Available MER in situ observations were used as ground truth to validate the interpretations of the Hapke parameters. Varied scattering properties were observed within a CRISM observation (5x10km) suggesting that the surfaces are controlled by local geological processes (e.g., volcanic resurfacing, aeolian and impact processes) rather than regional or global processes. Results are consistent with the in situ observations, thus validating the approach and the use of photometry for the characterization of Martian surface physical properties.

Citation: Fernando, J. et al. (2015), Characterization and mapping of surface physical properties of Mars from CRISM multi-angular data: application to Gusev Crater and Meridiani Planum, Icarus

1 Introduction

Planetary surfaces have been modified by a variety of geological and climatic processes, including external (e.g., space weathering), internal (e.g., volcanism) and interactions between surface and atmosphere (e.g., aqueous and wind erosion, alteration, transportation and deposition, CO_2 and H_2O cycles). These processes are recorded in the surface mineralogy and the surface texture. The mineral assemblage gives information about the chemical environment (e.g., crystallization from an igneous magma, deposition from aqueous agents, recrystallization due to metamorphism, crystallization during diagenesis process of sediments, oxidation and weathering of rocks due to interactions with the atmosphere). Analyses of particle physical properties (grain size, shape and internal structure) to its organization (surface porosity, roughness and grain size distribution) provide information regarding surface formation and evolution (e.g., the grain size discriminates volcanic and plutonic materials) including transportation (e.g., the grain shape reflects the history of the transportation and/or the capability of the erosion agent (liquid or wind) to erode the grains), deposition and weathering.

Measurement of the bidirectional reflectance in visible and near-infrared ranges at different geometries (incidence, emission and azimuthal angles) provides information about the scattering behavior. This scattering depends on the

composition and on the material physical properties: from the particle scale such as its size, shape, internal structure to its organization within a pixel such as the surface roughness and the grain size distribution. This technique has been used for the analysis of laboratory measurements (e.g., *McGuire and Hapke*, 1995; *Piatek et al.*, 2004; *Cord et al.*, 2005; *Shepard and Helfenstein*, 2007; *Pommerol et al.*, 2013; *Souchon et al.*, 2011; *Johnson et al.*, 2013), and for investigations conducted for Mars using in situ (e.g., *Johnson et al.*, 1999, 2006a,b, 2014) and orbital measurements (e.g., *Erard et al.*, 1994; *Jehl et al.*, 2008; *Fernando et al.*, 2013a; *Shaw et al.*, 2013). In situ measurements provide constraints on the scattering behavior from specific classes of rocks and soils at 10's of microns to 10's of meters scales and are limited to the rover path, whereas orbital measurements provide that information from more extended areas integrating rocks and soils (hectometer to kilometer spatial scales) and can be obtained everywhere on the planet. The High Resolution Stereo Camera (HRSC) on-board Mars Express (MEx) has acquired multi-angular (up to five geometries per orbit) data of the Martian surface. *Jehl et al.* (2008) determined the regional variations of the photometric properties at the kilometer spatial scale, across Gusev Crater and the south flank of Apollinaris Patera. They used several HRSC observations to enrich the diversity of available geometries (phase angle from 20 to 90°). Their photometric study was carried out without any atmospheric correction but ensuring that the atmospheric contribution was limited by selecting HRSC observations with mineral aerosol optical thickness lower than 0.9. Since 2006, the spectro-imager Compact Reconnaissance Imaging Spectrometer for Mars (CRISM) onboard Mars Reconnaissance Orbiter (MRO) provides multi-angular hyperspectral images (up to eleven geometries) giving access to the surface material scattering behavior at the hectometer spatial scale. Recently, *Fernando et al.* (2013a) proposed an approach to estimate the surface photometric parameters by inverting the Hapke photometric model (*Hapke*, 1993, 2012a), including a robust and fast atmospheric correction, called the Multi-angle Approach for Retrieval of the Surface Reflectance from CRISM Observations (MARS-ReCO) (*Ceamanos et al.*, 2013). The estimated photometric parameters provided information about the single scattering albedo and the main direction of the surface scattering (e.g., forward, backward) directly related to the physical state of the surface. Moreover, quantitative information regarding the surface roughness (roughness at microscales scales) could be provided. In parallel, *Shaw et al.* (2013) derived maps of the single scattering albedo and the scattering asymmetry parameter at MER-Opportunity landing site at Meridiani Planum, focused around the Victoria Crater, using CRISM multi-angular observations and a coupled surface and atmospheric model.

In this paper, we apply the methodology developed by *Fernando et al.* (2013a) to study the spatial variations of the scattering properties, as a function of mapped geological units, in terms of surface photometric parameters. We try to link the surface photometric parameters in terms of physical properties, by coupling with the orbital observations (e.g., CRISM/MRO spectral criteria, THermal EMission Imaging System (THEMIS) / Mars Odyssey thermal inertia values, High Resolution Imaging Science Experiment, (HiRISE)/MRO images and digital terrain model (DTM)), to provide information about the geological context. This work focuses on the Mars Exploration Rover (MER) landing sites, located at Gusev Crater and Meridiani Planum, where orbital and in situ observations are available. This application is an example of what the methodology and the mapping can provide as information about the surface material physical properties. The photometric results obtained from CRISM data are compared to the MER in situ observations (e.g., Panoramic camera (Pancam), Microscopic Imager (MI), Navigational camera (Navcam)), used as ground truth to validate the photometric interpretations.

The article is organized as follows: (i) the methodology to obtain the surface photometric parameters maps from the Hapke model is described in Section 2 and (ii) the analyses of these maps are presented and discussed by associating them with complementary orbital and in situ observations and with laboratory studies in Section 3. Then, we present (iii) the comparisons of the CRISM photometric results with a numerical model in Section 4 and (iv) the relations to the geological processes in Section 5.

2 Data sets and methods

2.1 CRISM targeted observations

The CRISM instrument on-board MRO is a visible and infrared hyperspectral imager (from 362 to 3920 nm at 6.55 nm/channel). The appropriate mode to estimate the surface spectro-photometric properties is the targeted mode. We decided to used the Full Resolution Targeted observations (FRT) which provide the highest spatial resolution (15-20m/pixel), and thus potentially less areal mixtures compared to lower resolution images. However, the Half spatial Resolution Long (HRL) and the Half spatial Resolution Short (HRS) observations could also be used by the methodology presented below. A targeted observation is a sequence of 11 hyperspectral images of a target area, acquired at different emission angles due to the rotation of the detector at ±70°. The solar incidence is almost constant during the spacecraft flyby over the target. The typical FRT sequence is composed of a central image (∼10x10 km) at high spatial sampling (15-20m/pixel) and 10 off-nadir images with a x10 binning (150-200m/pixel), taken before and after the central image, involving two azimuthal

modes (*Murchie et al.*, 2007).

2.2 Methodology

Fernando et al. (2013a) presented a methodology for the estimation of the Hapke photometric parameters from the CRISM multi-angular observations, summarized below. *Fernando et al.* (2013a) also presented a cross-validation of the methodology by comparing the CRISM estimates to the in situ photometric results at the MER landing sites. Compared to the previous works, the main goal in this work is to include the mapping of the surface photometric parameters in order to study the spatial variations of the scattering properties, as a function of mapped geological units, providing extended information over a wider area. This work also focuses on the physical interpretation of the modeled Hapke photometric parameters. The mapping induces same modifications in the previous methodology described in this subsection.

2.2.1 Integration of multi-angular images

The eleven hyperspectral images of a FRT observation (reflectance and ancillary cubes) are spatially rearranged into a new data set. We refer to this as a spectro-photometric curve (SPC) cube (*Ceamanos et al.*, 2013). In this work, the integration of the multi-angle images has been improved (i) by taking into account the geometric deformations (especially at oblique views) caused by the instrument rotation, and (i) by controlling the association between two pixels of two different images of the sequence. Both are not taken into account in the previous method (*Ceamanos et al.*, 2013). First, the central image, taken at 15-20m/pixel, is binned x10 to have the same spatial resolution as the 10 off-nadir images (150-200m/pixel). Second, all images are spatially combined to build the spectro-photometric curve of each spatial pixel, by spatially associating each pixel of the central image (chosen as reference) with pixels from the 10 off-nadir images. We calculate the spatial nearest pixel by using the spatial coordinates of each image of the FRT observation, and by taking into account the geometric deformation due to the detector gimbal (spatial resolution/cosine(emergence angle)). The association is performed when the overlapping between two pixels of two different images (central image and an off-nadir image) is at least 10%.

2.2.2 Correction for mineral aerosol contributions and estimation of the surface bidirectional reflectance

Ceamanos et al. (2013) proposed a technique, referred to as MARS-ReCO, to correct for mineral aerosols exclusively in order to estimate the surface bidirectional reflectance. For this work, the surface bidirectional reflectance is estimated at 750 nm where the contribution from gas is negligible. The optical properties of mineral aerosol (particle size distribution and refractive index) and the mineral and water ice aerosol optical thickness ($AOT_{mineral}$ and AOT_{water}) of each observation are provided by Michael Wolff (*Wolff et al.* (2009), personal communication, 2011). The $AOT_{mineral}$ for each CRISM acquisition is used as an input of MARS-ReCO. MARS-ReCO is able to propagate the uncertainties on the surface bidirectional reflectance from the top-of-atmosphere (TOA) measurements. The different criteria for the use of the MARS-ReCO approach are presented in Sub-section 2.3.

2.2.3 Estimation of Hapke photometric parameters

To analyze the surface bidirectional reflectance, the *Hapke* (1993, 2012b) model is used. This model depends on the geometric angles (incidence, emergence and phase angles) and on six parameters: the single scattering albedo, the particle phase function, the surface macroscopic roughness and the opposition effect parameters (Table 1). It is important to mention that CRISM is not observing Mars with phase angles less than 20°. Consequently, the opposition effect parameters (magnitude B_0 and angular width h of the opposition effect (Table 1)), are underconstrained. However, as explained by *Fernando et al.* (2013a), neglecting both parameters should not influence the retrieval of the other parameters. However, following *Souchon et al.* (2011), the model can still be profitably inverted by keeping parameters B_0 and h. We tested first by inverting the parameters B_0 and h to systematically control if they are constrained or not by the CRISM data set using the non-uniformity criterion (k) described in subsection 2.4. Second we tested the inversion by setting B_0 and h to zero, and no change was observed on the determination of the other parameters (ω, $\bar{\theta}$, b, and c).

The photometric parameters are estimated using a Bayesian inversion framework, adapted for the inversion of the non-linear Hapke model (*Fernando et al.*, 2013a,b). This technique is based on the concept of the state of information, characterized by a probability density function (PDF) (*Tarantola and Valette*, 1982). The prior information about model parameters (no information, defined as uniform PDF) combined with prior information about observations (a gaussian PDF) are fused to infer the solution by using Bayes' theory. The final state of information (posterior PDF of each parameter) is numerically sampled, using a Monte Carlo Markov Chain (*Mosegaard and Tarantola*, 1995), to calculate the posterior PDF and the mean and the standard deviation of each Hapke photometric parameter (see *Fernando et al.*

Symbole	Definition	Physical significance	Geological significance
ω	Single scattering albedo	ratio of scattered light at the particle scale to extincted light	particle composition and size and microstructure
b	Asymmetry parameter[a]	anisotropy of the scattering ($b < 0.5$: broad / $b \geq 0.5$: narrow scattering lobe)	particle shape, composition and internal structure
c	Backscattering fraction[a]	main scattering direction ($c < 0.5$: forward / $c \geq 0.5$: backward scattering)	particle shape, composition and internal structure
B_0	Magnitude of the opposition effect	magnitude of the opposition effect peak (g <5°)	particle transparency ($B_0 = 0$: transparent particle, $B_0 = 1$: opaque particle)
h	Angular width of the opposition effect	angular half width of the opposition effect peak (g <5°)	surface porosity, particle size ($h = 0$: high porosity, $h = 1$: low porosity and/or more uniform grain size distribution)
$\bar{\theta}$	Macroscopic roughness	mean slope angle within a pixel expressed in degree	roughness at microscale (from the particle to a few mm)

[a] We assume a two-term Henyey-Greenstein phase function (HG2)
g: phase angle

Table 1: Summary of the Hapke photometric parameters and their physical and geological significance. All parameters are depending of the wavelength, set to 750 nm in this work. Note that the parameters ω, b, c, B_0 and h vary from 0 to 1 and the parameter $\bar{\theta}$ varies from 0 to 45°.

(2013a,b) for more details). The advantages of this inversion procedure are that the the data uncertainties are taken into account in the model parameter estimations and all parameter assemblages are tested.

The single scattering albedo (ω) is related to the composition, the particle size and the microstructure (e.g., crystals, fractures, pores) (*Hapke*, 1993, 2012b). The phase function parameters (b and c) are dependent and are related to the particle shape, composition and internal structure (e.g., *McGuire and Hapke*, 1995; *Souchon et al.*, 2011). The macroscopic roughness ($\bar{\theta}$) parameter is initially defined as the integral surface roughness at the sensor subpixel scales (*Hapke*, 1993, 2012b). However, several authors demonstrated that the surface macroscopic roughness parameter is more sensitive to the microscale (from the particle size to a few millimeters) and thus to the grain organization (*Shepard and Campbell*, 1998; *Helfenstein and Shepard*, 1999; *Cord et al.*, 2003; *Shkuratov et al.*, 2005; *Shepard and Helfenstein*, 2007). In addition to the photometry technique, several techniques and approaches have been developed to estimate the Martian surface roughness, specially to have the access to the sub-meter scale morphology including, the laser altimeter measurements (e.g., *Neumann et al.*, 2003), the radar measurements (e.g., *Campbell*, 2001) and the surface temperature measurements (e.g., *Bandfield and Edwards*, 2008). However, all these approaches did not provide the same scale of surface roughness. The surface roughness is characterized at scales larger than about 300 m from laser altimeter measurements, like Mars Orbiter Laser Altimeter (MOLA) data, at centimeter to meters scales from radar observations, and at 0.01 m (for low thermal inertia to 0.1 m for moderate thermal inertia) from thermal infrared observations. Consequently, a direct comparison is not possible due to the different roughness scales but all are complementary.

2.3 Criteria for the selection of CRISM observations

Since September, 2010, the inbound segment in CRISM targeted mode is absent due to problems of the gimbal instrument (*Murchie*, 2012). In order to have the maximum number of geometries, only CRISM observations acquired before this date are selected.

The MARS-ReCO procedure is suitable for any CRISM observation within the following constraints described below.

(1) The accuracy of the determination of the surface reflectance highly depends on the combination of a moderate mineral aerosol opacity ($AOT_{mineral} \leq 2$, (*Ceamanos et al.*, 2013)) and a low water ice aerosol opacity, as the latter is not corrected by MARS-ReCO ($AOT_{water} \leq 0.2$, water ice content).

2) The accuracy of the determination of the surface reflectance highly depends on the geometries. The MARS-ReCO procedure is suitable for any CRISM multi-angular observation within these geometrical constraints: incidence angle $\theta_0 < 60°$, phase angle range $\Delta g = g_{max} - g_{min} > 40°$, outside the plane perpendicular to the principal plane ($\varphi_{inbound} = \varphi_{outbound} \sim 90°$) (*Ceamanos et al.*, 2013). The local topography makes the photometric study more challenging when it is poorly known, because it controls to a large extent, the incidence, emergence, and azimuth local angles. Besides,

in the case of an oblique illumination (i.e., up to 70°), shadows decrease the signal/noise ratio. Consequently, regions with steep surfaces which can be observed within a CRISM central image (10kmx10km) but which may create high shadows, are excluded for this work (e.g., the crater central peaks, slopes and rims, the channel slopes, the steep hills), to minimize the errors. The regions with high relief are evaluated from the high resolution HiRISE images or from the HiRISE digital terrain models and their photometric results are masked in the final maps.

The success of the MARS-ReCO procedure is evaluated by the percentage of corrected pixels. Observations with more than 50% of failed pixels after the MARS-ReCO procedure are rejected (a failed pixel means that the MARS-ReCO did not correct its photometric curve). The failure can be explained by the fact that one or several geometric and/or atmospheric conditions, detailed previously, is/are not respected.

2.4 Evaluation on the accuracy of the surface photometric parameters estimates

After the MARS-ReCO correction, we can evaluate if the surface photometric curve (especially the diversity and number of available geometries) provides enough information to estimate accurate Hapke photometric parameters. For that purpose, we analyze the shape of the posterior PDF. The criteria are summarized below.

(1) Non-uniformity criterion (k): A solution exists if the posterior PDF differs from the prior information (a uniform distribution). A statistical test is performed, leading to a non-uniformity criterion k (*Fernando et al.*, 2013a). For $k \geq 0.5$, the posterior PDF is considered to be a non-uniform PDF, meaning that a solution exists.

(2) Bimodality of the single scattering albedo PDF criterion: The presence of two possible solutions (e.g., bimodal distribution) for the ω parameter is the consequence of the limitation of geometric diversity in the CRISM photometric curve to constrain the ω parameter (*Fernando et al.*, 2013a,b), which is usually the best-constrained parameter in photometric modeling. Synthetic tests showed that if a pixel has a bimodal distribution for the ω parameter, generally one or several parameters has/have no solution or if a solution exists, this solution is underconstrained (i.e., high standard deviation) (*Fernando et al.*, 2013a,b). All pixels having a bimodal distribution for the ω parameter are not considered and the photometric parameter set are not used and not mapped.

(3) Standard deviation (σ) criterion: This is used to characterize the dispersion around the mean value, giving constraints on the accuracy of the solution. A solution is considered as well-constrained when $\sigma_\omega \leq 0.10$ for the ω parameter (which is the best constrained parameter in modeling), $\sigma_{b,c} \leq 0.20$ for the b and c parameters and $\sigma_{\bar{\theta}} \leq 5°$ for the $\bar{\theta}$ parameter (b, c and $\bar{\theta}$ are the less well-constrained parameters due the limited range of CRISM geometries).

The quality of the eleven multi-angular images comprising the region under study is crucial. Indeed, the ten off-nadir image footprints must ideally overlap the central image. However, due the surface topography uncertainty, the spacecraft position and attitude uncertainties, and the gimbal jitter of the instrument, the overlap among all images is not always ideal. Consequently, a worst quality of the image overlap reduces the number of available angular configurations and the phase angle range. Only pixels with at least seven angular configurations are used for the estimation of surface photometric parameters. Tests using synthetic data sets showed that the sampling of photometric curve with less than seven geometries (among those available with CRISM observations) is not sufficient to accurately constrain the photometric parameters.

If all the above criteria are not respected, that means that the diversity of geometries and the sampling of the surface bidirectional reflectance are not enough to constrain all the photometric parameters. The solution, proposed by *Pinet et al.* (2005); *Jehl et al.* (2008); *Fernando et al.* (2013a), is to combine several observations, acquired under varied illumination conditions (assuming no surface changes) to improve the diversity of geometries.

In spaceborne and laboratory photometric data sets, interplay between certain parameters can lead to the same photometric curve. For instance, *Shepard and Helfenstein* (2007) observed that other Hapke parameters (such as the opposition effect parameters and the phase function parameters) can mimic the phase angle effects of macroscopic surface roughness at small phase angles. To reduce this effect, several authors showed that a high diversity of geometries (a broad phase angle range containing low and high phase angles) is necessary for constraining as possible all the parameter set (e.g., *Helfenstein and Shepard*, 1999; *Shepard and Helfenstein*, 2007; *Cord et al.*, 2003). These degeneracy problem cannot be handled with usual inversion method based on criteria minimization, leading to one single solution. Therefore we applied a Bayesian inversion approach in order to test all possibilities and to keep all solutions (*Fernando et al.*, 2013a). Within this framework, the solution is described as a probability density function on the parameter space. We demonstrated that phase angles higher than 90 degrees and large phase angle ranges ($>$ 50 degrees) are required to limit the degeneracy in order to constrain all Hapke parameters (*Fernando et al.*, 2013a,b). In this work, all selected CRISM observations have an available highest phase angle $>$ 100 degrees, a wide range of phase angles (Table 2) and a number of geometries greater than 7, which all minimize the tradeoff between the model parameters. Moreover, the Bayesian inversion and the presented criteria enumerated above are suitable for evaluating the quality of the parameter estimates compared to the sampling and the diversity of geometries of the surface photometric curve.

		MER-Spirit	MER-Opportunity		
	ID	FRT#C9FB	FRT#B6B5	FRT#334D	FRT#193AB
Time	Acquisition date	2008-09-21	2008-07-08	2006-11-30	2010-06-09
	Ls(deg.)	130.321	96	142.97	102.16
Geometry	θ_0 (deg.)	63	56	55	56
	$\varphi_{in} - \varphi_{out}$ (deg.)	$\simeq$ 55 - 131	$\simeq$ 44 - 128	$\simeq$ 64 - 117	$\simeq$ 50 - 128
	g_{min}-g_{max} (deg.)	$\simeq$ 45 - 110	$\simeq$ 40 - 106	$\simeq$ 49 - 97	$\simeq$ 39 - 105
	Δg (deg.)	65	66	48	66
Atmosphere[1]	$AOT_{mineral}$ (900 nm)	0.25±0.03	0.35±0.04	0.35±0.04	0.31±0.03
	AOT_{water} (320 nm)	0.07±0.03	0.14±0.03	0.12±0.03	0.13±0.03
MARS-ReCO	uncorrected pixels (%)	9	33		13
	nb. of corrected pixels	868	1703		1492
Bayesian inversion	nb. of pixels with $k_b \geq 0.5$ (%)	100	99		100
	nb. of pixels with $k_c \geq 0.5$ (%)	100	99		89
	nb. of pixels with $k_{\bar{\theta}} \geq 0.5$ (%)	100	100		100
	nb. of pixels with $k_\omega \geq 0.5$ (%)	100	100		100
	nb. of pixels with a bimodality PDF for ω (%)	25	11		17
	nb. of pixels with $\sigma_b \leq 0.20$ (%)	55	72		80
	nb. of pixels with $\sigma_c \leq 0.20$ (%)	72	51		36
	nb. of pixels with $\sigma_{\bar{\theta}} \leq 5°$ (%)	78	43		42
	nb. of pixels with $\sigma_\omega \leq 0.1$ (%)	100	100		97

Ls: Solar longitude, θ_0: incidence angle, $\varphi_{in} - \varphi_{out}$: CRISM inbound and outbound azimuthal angles, g_{min}-g_{max}: minimum and maximum of the phase angles, Δg: phase angle range, $AOT_{mineral}$: mineral aerosol optical thickness, AOT_{water}: water ice aerosol optical thickness, ω: single scattering albedo, b: asymmetric parameter, c: backscattering fraction, $\bar{\theta}$: macroscopic roughness, conf.: angular configurations, k: non-uniform criterion, σ: standard deviation, PDF: probability density function, [1]from Wolff's estimates (*Wolff et al.*, 2009, personal communication)

Table 2: Selected CRISM FRT observations at the MER-Spirit's and MER-Opportunity's landing sites, respectively at Gusev Crater and Meridiani Planum with information about geometric, atmospheric conditions and statictic results relative to the MARS-ReCO procedure and to the Bayesian inversion of the Hapke model.

3 Results of CRISM photometric maps

3.1 MER-Spirit landing site at Gusev Crater

3.1.1 Selection of CRISM observations

Up to eleven FRT observations are available at the MER-Spirit landing site from the beginning of CRISM operations to September 2010. Among all, the observation FRT#C9FB shows the best satisfactory statistical results relative to the MARS-ReCO procedure and to the Bayesian inversion (satisfactory values of the non-uniform criterion (k), the standard deviation criterion (σ) and the bimodality of the single scattering albedo PDF criterion) (Table 2). The solutions estimated from the observation FRT#C9FB are used in this study.

3.1.2 Geological context and study areas

Gusev Crater is an impact structure from the Noachian epoch, approximately 160 km in diameter and centered at 14.5° S/175° E (*Kuzmin et al.*, 2000). Previous studies suggested past fluvial and lacustrine activity from the 800-km long canyon Ma'adim Vallis, with sediment deposition that was at least partly responsible for the formation of the Columbia Hills (*Kuzmin et al.*, 2000; *Cabrol et al.*, 2003). However, some other authors recognized multiple eruptions of fluid basalts (*Greeley et al.*, 2005a), analogous to mare basalts (*Greeley et al.*, 1993). The region is also affected by seasonal aeolian processes. Hundreds of dark-toned, small sub-parallel streaks are observed. The tracks represent the removal of fine, bright-toned materials (consistent with dust (*Martinez-Alonso et al.*, 2005)) from the basaltic underlying dark-toned materials by dust devils (*Greeley et al.*, 2003) and/or storms.

The context region of our work is presented in Figure 1: the selected CRISM FRT#C9FB observation is presented in Figure 1a and the geological map, summarizing the different units and structures observed in the coupled HiRISE image (Figure 1b), is illustrated in Figure 1c. The HiRISE DTM image was used to calculate the mean slope at the meter per pixel (Figure 1d). Two units are discernible: the hills (Figure 1c in brown color), and the flat plain which is heavily cratered (referred to as Gusev cratered plain). Since the hills present high local slopes, it would require additional topographic modeling (beyond the scope of the current effort) to warrant their inclusion in the models. As such, this unit is masked in all subsequent model results. In detail, three units are observed:

(1) a dark-toned large band (NW-SE direction) associated with a dust storm track, referred to as "dark band feature" (Figure 1c, in green color),

(2) a region composed of numerous dark sub-parallel linear features (W-E direction) associated with dust devil tracks, referred to as "dark linear features" region (Figure 1c, in yellow color),

(3) a bright-toned region is observed in the NE and SW part of the CRISM observations, referred to as "bright-toned" region (Figure 1c, in red color).

The thermal inertia (TI) provides constraints on the bulk density, the particle size and the cohesion. From thermal emission imaging system (THEMIS) onboard Mars Odyssey, the average TI was estimated as 240 ± 20 $J.m^{-2}.s^{-0.5}.K^{-1}$ (spatial resolution of 100m/pixel) by *Milam et al.* (2003). The authors interpreted it as surface of medium-sized grain of sand. This value is associated with the Low Albedo (LA_t) unit (*Milam et al.*, 2003), the region where the selected CRISM observation is located.

In situ observations acquired by the MER-Spirit rover provide information about the surface physical and chemical properties from meter- to millimeter- scales of main geological units. *Arvidson et al.* (2006a) and *Arvidson et al.* (2008) provided an overview of key observations of soils and rocks. Along the traverse in the Gusev plains (Figure 2), images showed that the soil is composed of: (i) basaltic material excavated from lava flows by local impacts (*Greeley et al.*, 2005a), (ii) a layer of dark coarse sands and granules (0.5 to a few mm in diameter) (*Herkenhoff et al.*, 2004a; *Herkenhoff, K. E., et al.*, 2006) (Figure 2c, top), interpreted to be rich-olivine basalts (*Bell et al.*, 2004; *Christensen et al.*, 2004; *McSween, H. Y. et al.*, 2004), (iii) subangular lithic fragments, interpreted to be ejecta deposits, which are associated with the numerous craters, composed of clasts and rocks, and (iv) all coated with bright fine-grained materials, inferred to be dust with particles from silt ($< 4\ \mu m$ in diameter) (*Lemmon et al.*, 2004) to fine sand (mostly less than 150 μm), forming dust aggregates, (*Herkenhoff et al.*, 2004a; *Sullivan et al.*, 2008; *Vaughan et al.*, 2010) (Figure 2c, bottom).

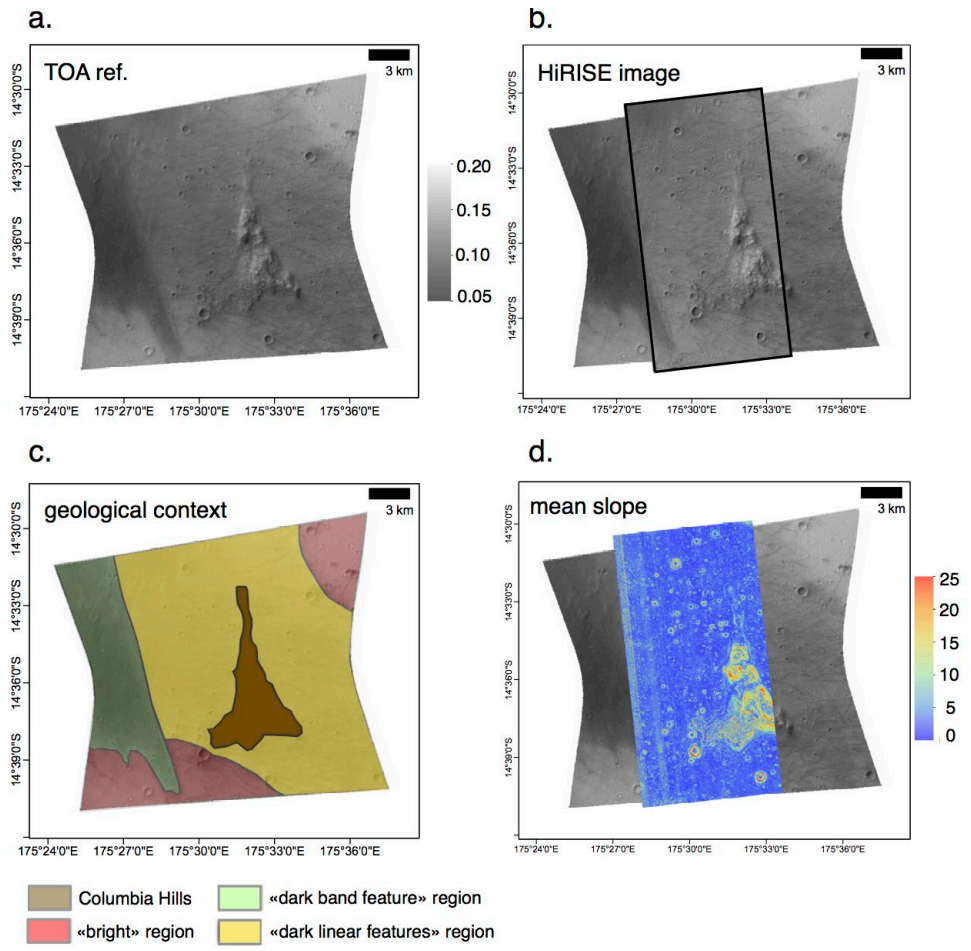

Figure 1: Geological context and studied area: a. CRISM top-of-atmosphere (TOA) central images (FRT#C9FB) at 20m/pxl at 750 nm, b. CRISM TOA central images overlapped by the associated HiRISE image (PSP_010097_1655_RED), c. CRISM TOA overlapped by geological context map showing the different units and structures, d. CRISM TOA overlapped by the mean slope map at 1 m derived from HiRISE Digital Terrain Model (DTM) (DTEEC_001513_1655_001777_1650_U01).

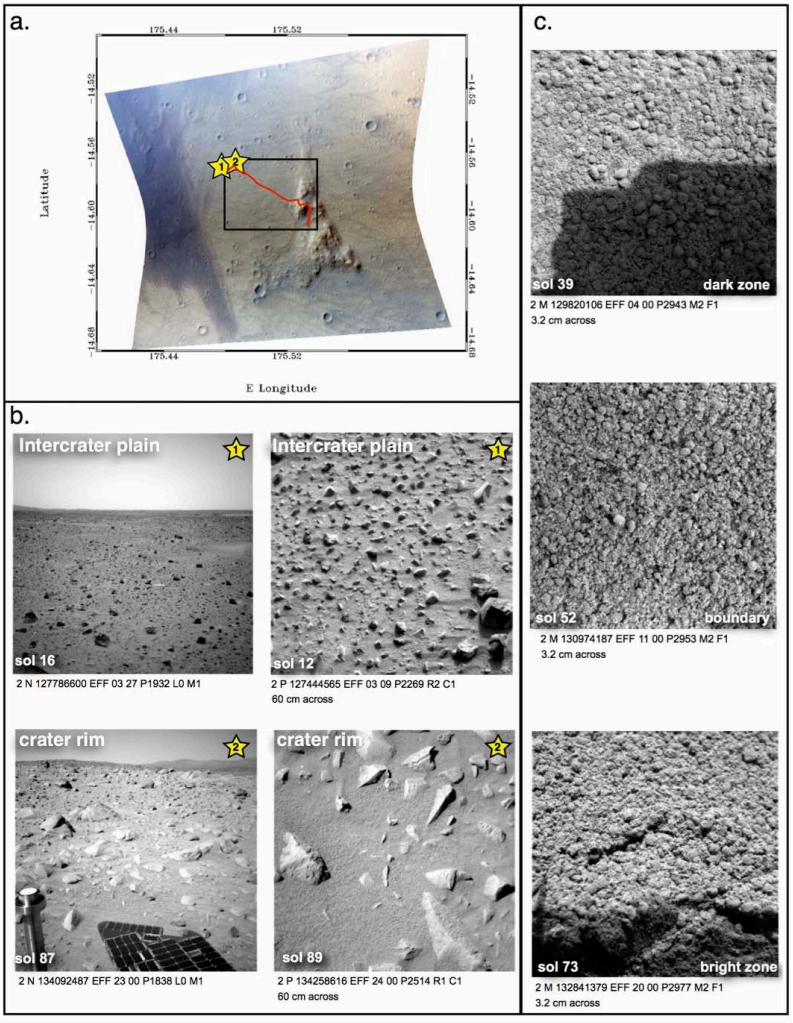

Figure 2: In situ observations from navigational camera (Navcam)/MER (N), Panoramic camera (Pancam)/MER (P) and Microscopic Imager (MI)/MER (M). (a) FRT#C9FB RGB image at ∼20m/pxl (credit: http://crism-map.jhuapl.edu/) with the rover path (in red color) and the locations of selected in situ images (location 2 is near Bonneville crater), (b) Navcam and Pancam images in the intercrater region (top) and near crater rim (bottom) and (c) MI images focused on inside a dust devil track (top), in the boundary (middle), and outside the dust devil track (bottom).

3.1.3 Surface material photometric parameters

3.1.3.1. The single scattering albedo parameter

Figure 3b represents the map of the single scattering albedo parameter (ω) values. Spatial variations of the ω parameter are observed at ∼200 meters CRISM scale: (i) the "dark band feature" region (Figure 1c, in green color) is correlated to the lowest ω values ($\omega < 0.60$, $\sigma \leq 0.10$), (ii) the "dark linear features" region (Figure 1c, in yellow color) is correlated to intermediate ω values ($0.65 < \omega < 0.75$, $\sigma \leq 0.10$), (iii) the "bright-toned' region (Figure 1c, in red color) is associated with the highest ω values ($\omega > 0.75$, $\sigma \leq 0.10$).

The ω values estimated from CRISM ($\omega_{CRISM} \simeq 0.65 - 0.75$) are compared to those estimated from Pancam measurements at 753 nm, located in our "dark-linear feature" geological unit, for different geological units (rocks and soils) (*Johnson et al.*, 2006a) (Figure 4a). The ω values are consistent with those obtained at Bonneville Rim site ($\omega_{\ Pancam} \simeq 0.66$), Landing Site and NW of Missoula areas ($\omega_{\ Pancam} \simeq 0.75$).

Orbital observations showed that the Gusev Crater plain is composed of basalt, detected in the thermal infrared range by the Thermal Emission Spectromer (TES) instrument (*Milam et al.*, 2003). Moreover, nanophase ferric-oxide-

rich (npOx) bright dust is detected, which partially covers the basaltic substrate detected by the Observatoire pour la Minéralogie, l'Eau, les Glaces et l'Activité (OMEGA) instrument over the MER-Spirit landing site (*Lichtenberg et al.*, 2007). Those results were confirmed by the in situ observations. To assess the distribution of surface dust, the nanophase ferric oxide (npOx) spectral index was calculated from the CRISM data set and mapped (Figure 5). Based on the presence of a broad near-infrared absorption between 0.75 and 1.0 μm due to the Fe^{3+} electronic transitions, the spectral ratio of the reflectance at wavelengths 1 μm and 0.8 μm is calculated (so called 1/0.8 μm slope) to estimate the nature of ferric oxide (*Poulet et al.*, 2007). Values close to 1 or greater are related to the high contamination of dust which masks the underlying materials. However, the npOx index is not corrected for mineral aerosol contribution, and is therefore sensitive to the mineral aerosol content in the atmosphere. The $AOT_{mineral}$ estimated for the FRT#C9FB is relatively low (0.25±0.03, Table 2), which suggests that the highly structured spatial distribution of dust index in Figure 5, dominantly shows surface signal.

By comparing the reflectance map at 750 nm (Figure 3a) and the ω map (Figure 3b) to the dust index map (Figure 5), three photometric regions are distinguishable. The region composed of "dark band feature" (Figure 1c, in green color) is correlated to the lowest dust signature (npOx $\simeq$ 0.90). This region is correlated to the lowest ω values ($\omega_{CRISM} \simeq$0.60, $\sigma \leq 0.10$). The "bright-toned" region in NE of CRISM observation (Figure 1c, in red color) shows high dust signature (npOx close to 1) and the highest ω values ($\omega_{CRISM} \simeq 0.80$, $\sigma \leq 0.10$). The region around and on the Columbia Hills ("dark linear features" region) (Figure 1c, in yellow color) is correlated to intermediate dust index values (npOx $\simeq$ 0.95). This likely results from the surface dust, partly contaminating the substrate, resulting in a mixed signal from dust and basalt. This area is correlated to intermediate ω values ($\omega_{CRISM} \simeq$ 0.65-0.75, $\sigma \leq 0.10$).

The single scattering albedo value decreases with the absorption coefficient: for a given particle size, a high absorption coefficient provides a low single scattering albedo value. At the studied wavelength (750 nm), similar optical constants (n, the refractive index and k, the absorption coefficient) are observed between the typical Martian dust (n=1.50, k=0.001, estimated from CRISM observation (*Wolff et al.*, 2009)) and a typical basalt (n=1.52, k=0.0011, estimated from laboratory measurements (*Pollack et al.*, 1973)). Consequently, the spatial variation of the parameter ω, observed in Figure 3b, cannot be explained solely by a composition variation.

The single scattering albedo value increases when the particle size decreases. Because dust and basalt have very close optical constants, the highest ω values in the "bright-toned' region can be explained by the presence of finer particles, compared to the region of "dark band feature", consistent with the in situ observations (Figure 2). Intermediate ω values are observed in the region with numerous dust devil tracks with a width less than 100 meters, which is lower than the CRISM spatial resolution (∼200m/pixel). As such signal of some CRISM pixels may be a mixed signal between dust and basaltic sands. Indeed, along its traverse, the rover crossed albedo boundaries observed from Pancam images: low-albedo dust devil tracks (0.20±0.02) and high-albedo dustier deposits (0.30±0.02) (*Bell et al.*, 2004). From the high resolution MI images of the soils on the aeolian features, *Greeley et al.* (2004, 2005b) provided explanations for these albedo contrasts as follows. Inside the track, dust is partly removed and the underlying basalt is observed as coarse sand grains ($\simeq$ 1 mm in diameter). Some dust particles remain resulting in an intimate mixture (Figure 2c, top). Outside the tracks, a relatively thick dust cover may remain on the top of the basalt in a stratified mixture (Figure 2c, bottom). In the transition of outside and inside the tracks, a spatial mixture of both units may be detected.

The in situ observations from the MI instrument showed that dust particles are often observed as aggregates of individual unresolved finer particles (*Herkenhoff et al.*, 2004a; *Sullivan et al.*, 2008; *Vaughan et al.*, 2010), where the subparticles can act like internal scatterers and increase the single scattering albedo.

The spatial variation of ω parameter seems to be related at first order to the spatial variation of the particle size. This variation is caused by the dust removal (decrease in the ω values) and deposition (increase in the ω values) by aeolian processes by strong winds such as storms (such as the "dark band feature" region) or dust devils where silt-sized and sand-sized materials can be removed in suspension and by active saltation (*Greeley et al.*, 2006). The ω values in the "dark linear feature" region result from a mixture (stratified, intimate, spatial) between basalt and dust (Figure 2c), as is tested by numerical modeling in subsection 4.2.

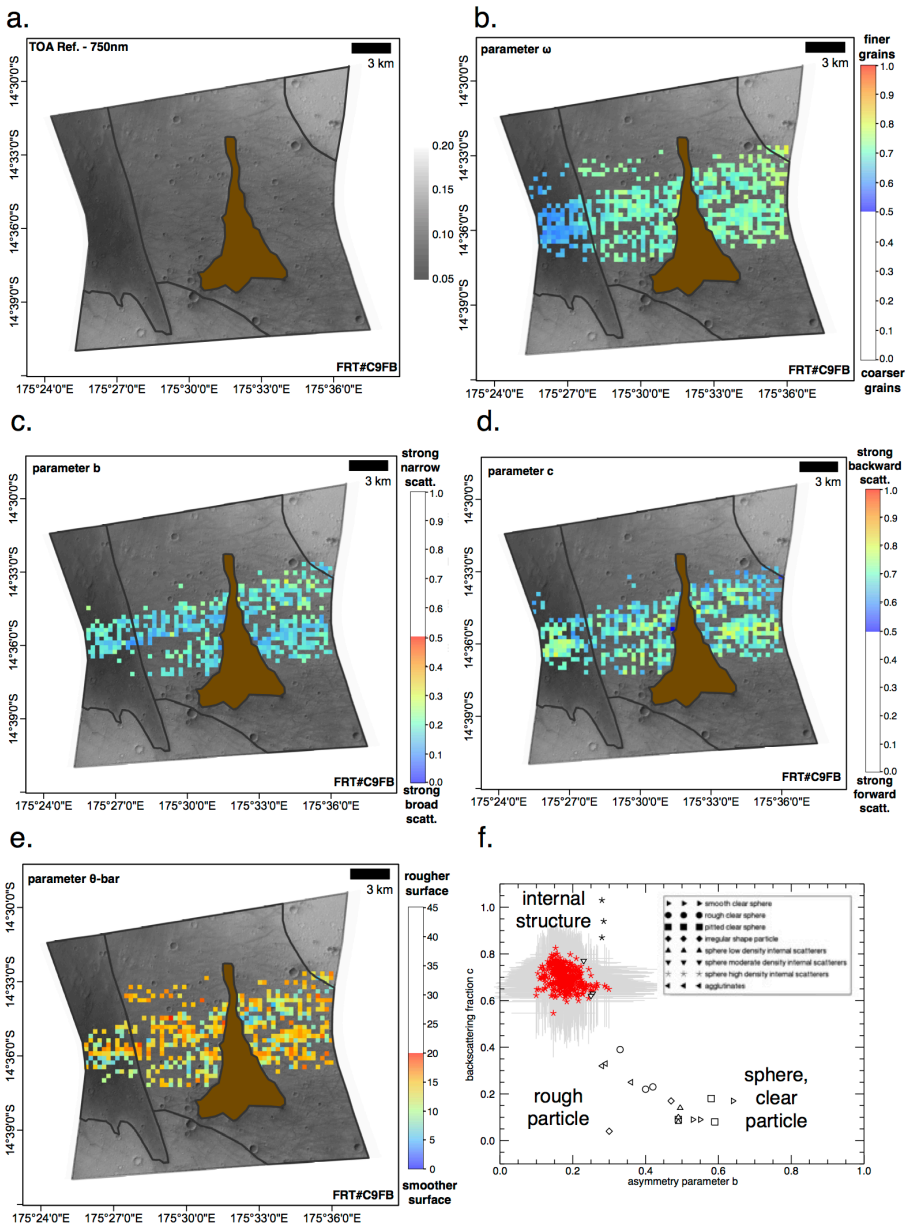

Figure 3: CRISM mapping (FRT#C9FB). a. TOA reflectance map in I/F unit at 20m/pixel at 750 nm. b. parameter ω map at 200m/pixel ($\sigma_\omega \leq 0.10$). c. parameter b map at 200m/pixel ($\sigma_b \leq 0.20$). d. parameter c map at 200m/pixel ($\sigma_c \leq 0.20$). e. parameter $\bar{\theta}$ map at 200m/pixel ($\sigma_{\bar{\theta}} \leq 5°$). The colored pixels correspond to the value of the mean PDF. Only the middle part of the central image is covered with all additional geometric images (up to 11 images) that it is why the photometric results are obtained in this area. f. graph of the asymmetry parameter (b) versus backscattering fraction (c) estimated from FRT#C9FB plotted with experimental values on artificial particles from *McGuire and Hapke* (1995). Note that the results in the hills unit are masket out due to high local topography.

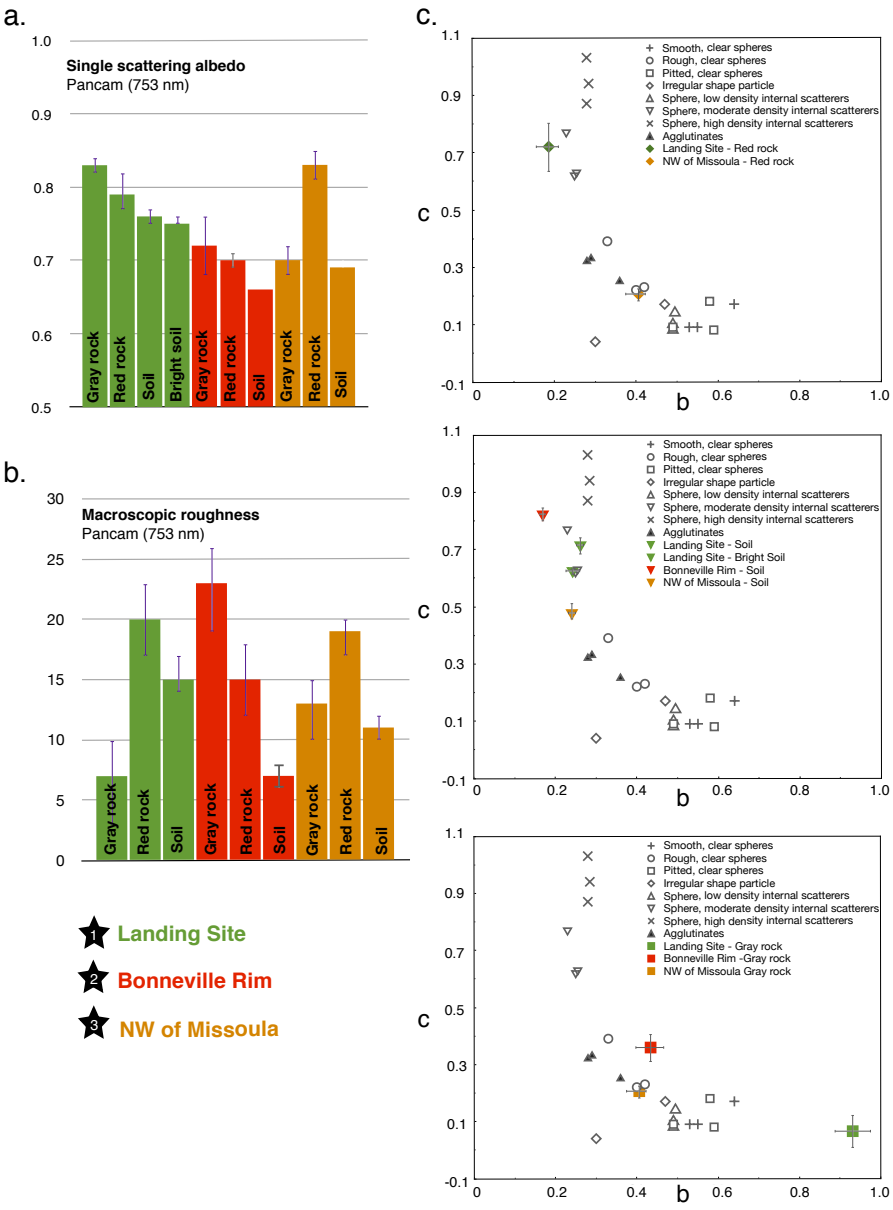

Figure 4: In situ photometric results from Pancam/MER: Mean and uncertainties of a. the single scattering albedo (ω), b. the macroscopic roughness ($\bar{\theta}$), c. the particle phase function parameters (b and c) overplot to the experimental b and c values pertaining to artificial particles measured by *McGuire and Hapke* (1995). All photometric parameters are estimated at 753 nm (except for the parameter c of Red Rock unit for landing site which corresponds to the 754 nm model results) from Pancam onboard Spirit for different geological units at Landing Site (Sol 013), Bonneville rim (Sol 087-088), and NW of Missoula (Sol 102-103) (*Johnson et al.*, 2006a).

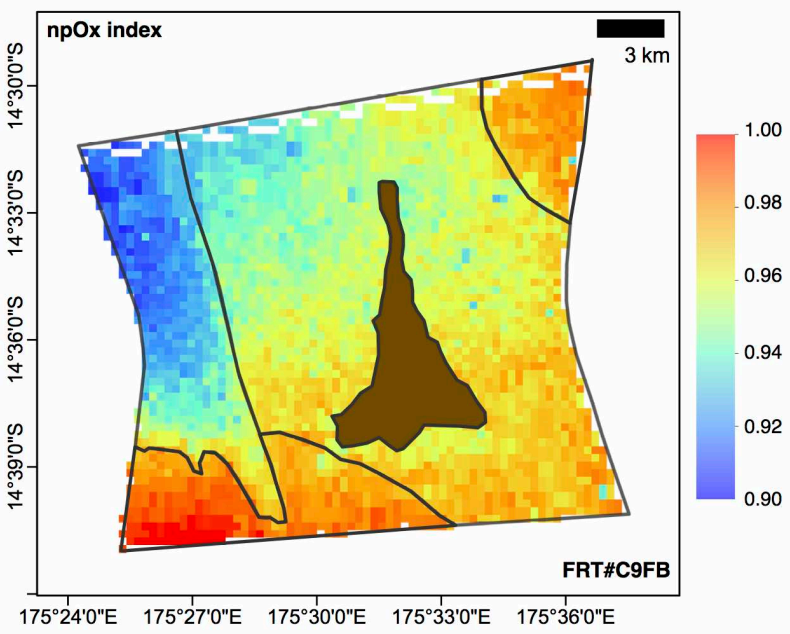

Figure 5: Composition map of nanophase ferric oxide spectral index (dust index) from FRT#C9FB: low or no dust areas have dust index less than 1 (blue tones) whereas dusty region have dust index greater or equal to 1 (red tones). The spatial resolution is 200m/pixel.

3.1.3.2. The particle phase function parameters

Figures 3c and 3d present the mean values of the posterior PDF for asymmetry parameter (b) and the backscattering fraction (c), respectively. The c parameter values show backscattering behavior (> 0.5) and the parameter b values indicate broad scattering lobe (< 0.5) for all pixels (Figures 3c, 3d and 3f). The local differences in the map are not significant in comparison to the error ($\sigma < 0.2$).

By comparing to the in situ photometric results, the CRISM results are consistent with b and c values, estimated for Soil unit at the Landing site and the Bonneville Rim sites (*Johnson et al.*, 2006a) (Figure 4c).

To provide a physical meaning of the phase function parameters, experimental studies were conducted on well-characterized natural and artificial materials (*McGuire and Hapke*, 1995; *Shepard and Helfenstein*, 2007; *Souchon et al.*, 2011; *Johnson et al.*, 2013). *McGuire and Hapke* (1995) studied the scattering properties of different isolated artificial particles which had different structure types. Their study showed that smooth clear particles exhibit greater forward scattering (low values of c) and narrower scattering lobes (high values of b), whereas particles characterized by their roughness or internal scatterers exhibit greater backward scattering (high values of c) and broader scattering lobe (low values of b) (Figure 3f). By comparing to the *McGuire and Hapke* (1995)'s study, the scattering properties acquired from the CRISM observation are closer to the scattering properties of artificial materials composed of particles with moderate density of internal scatterers (Figure 3f). Similarly, *Souchon et al.* (2011) measured, for a comprehensive set of geometries, the reflectance factor of natural granular surfaces composed of volcanic materials differing by their grain size, shapes, surface aspect, and mineralogy (including glass and minerals). By comparing to the *Souchon et al.* (2011)'s work on natural volcanic samples, the scattering properties of "dark band" region where basaltic sands are exposed (Figure 1c, in green color), are closer to the scattering behavior of pyroclastics from Towada T6 (425-1000 μm), characterized by rounded grains with rough, hollowed and opaque surfaces, with facets of phenocrysts and some isolated crystals. The results show that the grains at the Gusev plain are consistent with rounded grains which are transported in long distance by wind. Second, the results show that the grains are composed of a high density of internal scatterers, suggesting the presence of either high density of crystals and/or the presence of impurities (e.g., bubbles) and/or fractures.

The MI images focused on a typical basaltic soil of coarse grains and cleaned of dust (Figure 2c, top) showed rounded and relatively spherical sands and granules, as shown by *Greeley et al.* (2006). Moreover, the basaltic materials showed a complex and heterogeneous structure created by different crystals (e.g., olivine, pyroxene, plagioclase) that may cause the observed backward scattering behavior. Those results are consistent with the b and c values estimated from the CRISM observation.

3.1.3.3. The surface macroscopic roughness parameter

Figure 3e represents the map of the macroscopic roughness parameter ($\bar{\theta}$) values. High $\bar{\theta}$ values ($\bar{\theta}$ ∼15-20°, $\sigma \leq 5°$) are observed.

To explain the high $\bar{\theta}$ values, the mean slope was calculated from the HiRISE DTM at scale of 1 meter per pixel (Figure 1d). In the cratered plains, we can identify 0.1-1 km diameter-size craters characterized by the highest mean slope (mean slope: 5 - 10°). The intercrater plain is characterized by the lowest mean slope (mean slope: $< 5°$) (Figure 1d). By comparing the $\bar{\theta}$ parameter map to the mean slope, we note that the high $\bar{\theta}$ values are not correlated with a high mean slope. This suggests that the macroscopic roughness parameter is not representative of the local topography at the meter- scale. The $\bar{\theta}$ parameter is more sensitive to the microscale (from the particle size to a few millimeters) and thus to the grain organization, as suggested by *Shepard and Campbell* (1998); *Helfenstein and Shepard* (1999); *Cord et al.* (2003); *Shkuratov et al.* (2005); *Shaw et al.* (2013).

Average surface macroscopic roughness values, obtained from CRISM data (∼13° ± 4° Figure 3e) are close to those estimated from in situ photometric observations (∼14° ± 2°, Figure 4b) from Pancam (*Johnson et al.*, 2006a). This suggests that the macroscopic roughness, estimated from CRISM data, is more representative of the microscale of the soil unit in agreement with earlier findings based on HRSC data (*Jehl et al.*, 2008).

The HiRISE image may also provide information about the surface morphology and the surface roughness. The HiRISE image (Figure 1b) shows numerous craters which may be accompanied by angular mm- to cm-sized ejected clasts and rocks. The high population of such ejecta materials having an angular shape may create a high shadow hiding, leading to a high macroscopic roughness values (Figure 6).

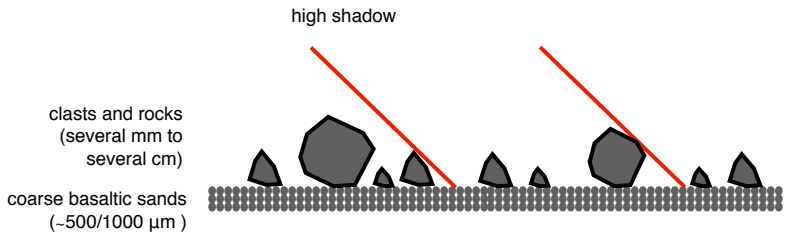

Figure 6: Schematic representation of the meaning of the macroscopic roughness values and the relation to the surface roughness in the Gusev plain. (∼ 500 μm for basaltic sands and several millimeters to several hundreds centimeters for the clastes and rocks).

3.2 MER-Opportunity landing site at Meridiani Planum

3.2.1 Selection of CRISM observations

Up to seven FRT observations are available at MER-Opportunity landing site from the beginning of the CRISM operations to september 2010. Among all, the observations FRT#B6B5 and FRT#193AB show the best statistic results, relative to the MARS-ReCO procedure, and the Bayesian inversion (satisfactory values of the non-uniform (k), the standard deviation (σ) criteria and the bimodality of the single scattering albedo PDF criterion). However, the statistic results for the parameter c of the observation FRT#B6B5 show a number of pixels with $\sigma_c \leq 0.20$ equal to 8%. To improve the geometric diversity of the FRT#B6B5, we combined the observations FRT#B6B5 and FRT#334D because they are superimposed, have complementary geometric acquisitions, and no obvious surface changes were observed. After the combination, the statistics of Bayesian inversion are improved, especially for the parameter c, showing a number of pixels with $\sigma_c \leq 0.20$ equal to 25%. The solutions, estimated from the combination of FRT#B6B5 and FRT#334D and from FRT#193AB, are presented in this work (Table 2).

3.2.2 Geological context and study areas

The MER-Opportunity landed in the Plains, Hematite-bearing (Ph) unit composed of patches light-toned sedimentary materials (etched terrain, ET2), overlain by a unconsolidated veneer of crystalline hematite bearing (plains mantle, Pm), detected by the TES instrument (*Christensen et al.*, 2000, 2001).

Two sites are presented in this work: the surrounding of the Victoria crater (results from the combination of FRT#B6B5 and FRT#334D observations, called area 1), and the West side of Endeavour crater rim (results from the FRT#193AB observation, called area 2) (Figure 7a).

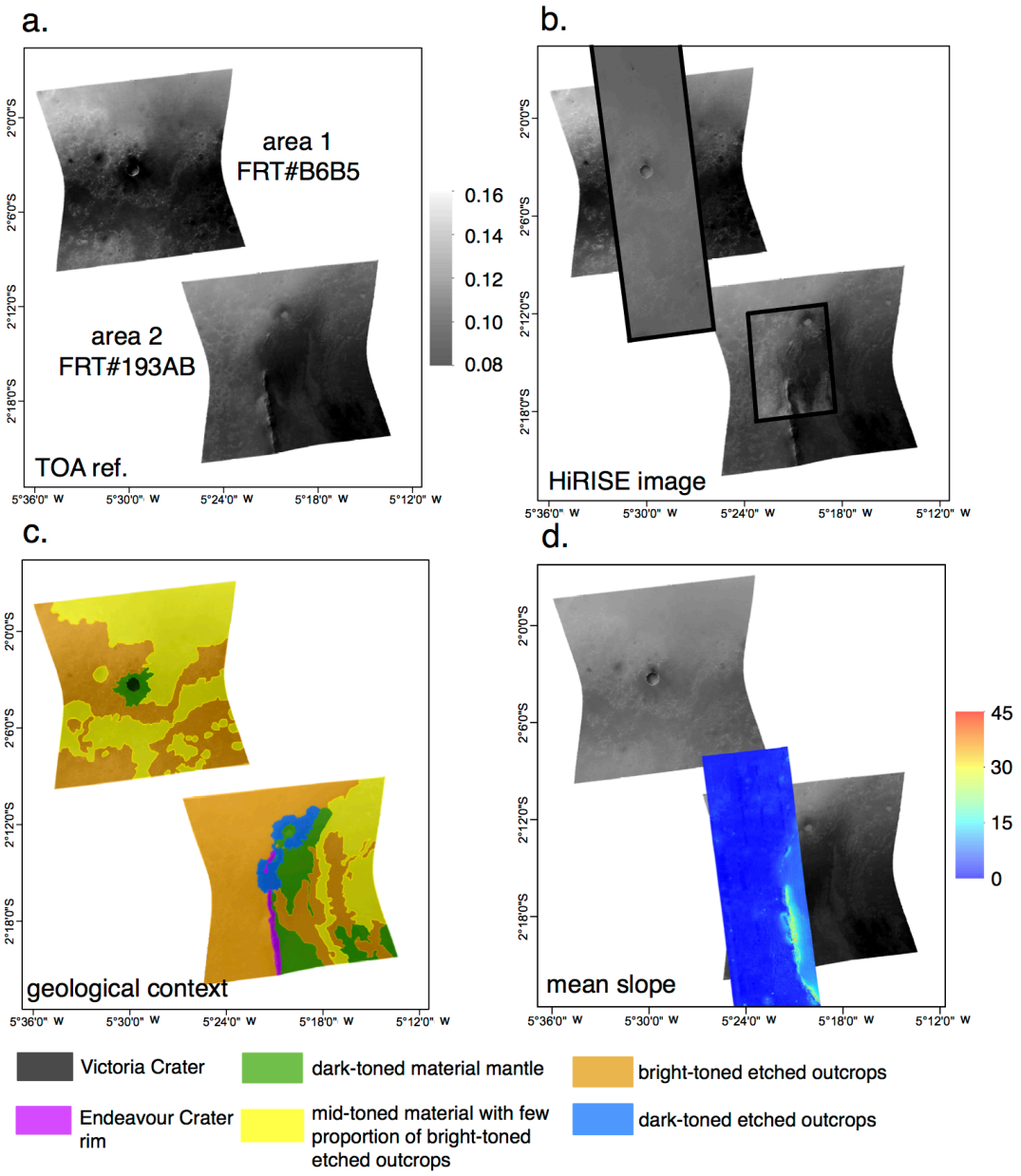

Figure 7: Geological context and studied area: a. CRISM TOA central images (FRT#B6B5 and FRT#193AB) at 20m/pxl at 750 nm, b. CRISM TOA central images overlapped by the associated HiRISE image (PSP_009141_1780_RED and ESP_032573_1775_RED), c. CRISM TOA overlapped by the geological context map showing the different units and structures, d. CRISM TOA overlapped by the mean slope map at 1m derived from HiRISE Digital Terrain Model (DTM) (DTEEC_018701_1775_018846_1775_U01).

Victoria crater (area 1) The HiRISE image, taken at the same local time as the FRT#B6B5, was used to make the geological context map. Four geological units are discernible in the plains:

(1) Victoria crater (Figure 7c, black color unit),

(2) dark-toned materials mantle, around the Victoria crater (Figure 7c, green color unit),

(3) no or low extended areas of bright-toned materials in the aeolian ripple troughs, corresponding to the bedrock (etched terrain) associated with mid-toned materials in the ripple crests (Figure 7c, yellow color unit),

(4) high extended areas of bright-toned materials in the aeolian ripple troughs, corresponding to the bedrock (etched terrain), associated with mid-toned materials in the ripple crests (Figure 7c, orange color unit).

Orbital reflectance spectra acquired by OMEGA on-board MEx, over the MER-Opportunity landing site, are dominated by a basaltic sand cover mixed with crystalline hematite and small amount of dust (*Arvidson et al.*, 2006b). The

abundant hydroxylated and hydrated sulfate minerals, observed by the rover (*Arvidson et al.*, 2011; *Squyres et al.*, 2006), corresponding to the brighter terrains (Figure 7c, red and orange color units) are identified in high resolution images (Figure 7b) but have not been detected over the landing site at the OMEGA and CRISM spatial resolution scales. The region dominated by ripples plains is characterized by low THEMIS TI values (∼140 - 145 $J.m^{-2}.K^{-1}.s^{-1/2}$ (*Arvidson et al.*, 2011)), suggestive of the presence of fine-grained aeolian materials. The region where bedrock is visible, the THEMIS TI values are slightly higher than ripples, suggestive of the presence of indurated materials (*Arvidson et al.*, 2011).

Squyres et al. (2006) and *Arvidson et al.* (2011) provided an overview of key observations of soils and rocks observed by MER-Opportunity. Along the rover traverse (Figure 8a), the in situ observations showed that the Meridiani plain surfaces are covered by aeolian ripples (Figure 8b, top). The soil in the ripple troughs is dominated by rounded hematitic concretions, and fragments and their size is larger than those found in ripple crest soils (Figure 8), whereas the soil in the ripple crest is dominated by well-sorted hematitic concretions of a relatively uniform size distribution (Figure 8) (granule : 1-2 mm in diameter). A few millimeters beneath the lag of deposit, the interior is dominated by a mixture of basaltic sands, fragments of hematitic concretions and dust (*Arvidson et al.*, 2006a; *Herkenhoff et al.*, 2004b; *Herkenhoff, K. E., et al.*, 2006; *Jerolmack et al.*, 2006; *Soderblom et al.*, 2004; *Weitz et al.*, 2006; *Squyres et al.*, 2004b, 2006; *Sullivan et al.*, 2005) (Figure 8b, top row). From the Erebus Crater to the Endeavour crater (Figure 8a), bright-toned flat-lying bedrock outcrops (Figure 7c, in orange color units) are visible and are exposed in ripple troughs, underlying the thin plain soil. The bedrocks are characterized by fine laminations, have a high concentration of sulfur and contain abundant sulfate salts (Figure 8b, middle line) (*Squyres et al.*, 2004b). MI images showed that the outcrops bedrocks are composed of: (i) moderate rounded well-sorted sand grains (from 0.2 to 1 mm) forming mm-scale laminations, (ii) fine-grained and coarser precipitated cement crystals, (iii) cm-sized vugs that record the early diagenetic growth and subsequent dissolution of crystals, and (iv) 3- to 5-mm sized hematitic spherules embedded within the outcrops (*Herkenhoff, K. E., et al.*, 2006; *Squyres et al.*, 2004c).

West side of Endeavour crater rim (area 2) The HiRISE image, taken at the same local time as the FRT#193AB, was used to make the geological context map.

At the west part of the rim in the Meridiani plain, the region is dominated by patches of bright-toned materials in the aeolian ripple troughs, corresponding to the bedrock (etched terrain), associated with mid-toned materials in the ripple crests (Figure 7c, orange color unit). This unit is the same as the etched terrains observed in the plains around the Victoria Crater. However, the unit is characterized by higher THEMIS TI values (∼155-180 $J.m^{-2}.K^{-1}.s^{-1/2}$ (*Arvidson et al.*, 2011)) in this area. The mean slope values derived from HiRISE DTM show low slopes, less than 5° (Figure 7d).

The region around the Endeavour Crater rim, including the Botany Bay area around the Cape York region (Figure 7c, blue color unit), is composed of dark-toned outcrops (etched terrain), visible in the HiRISE image (Figure 7b), detected to be hydrated sulfate-rich bedrocks from CRISM spectra (*Wray et al.*, 2009), and corresponding to the Burns formation sulfate-rich sandstones (*Arvidson et al.*, 2014).

The discontinuous Endeavour rim (Cape York in the north and Cape Tribulation in the south) (Figure 7c, purple color unit) shows the highest THEMIS TI values (>340 $J.m^{-2}.K^{-1}.s^{-1/2}$ (*Chojnacki et al.*, 2010)), suggestive of the presence of indurated materials (*Arvidson et al.*, 2011; *Chojnacki et al.*, 2010). The rim exposes basalt and iron and magnesium-rich smectite clay minerals (*Wray et al.*, 2009). The mean slope values, derived from HiRISE DTM, show high slopes, greater than 15° (Figure 7d).

The Endeavour crater floor is composed of several units:

(1) a mantle of dark-toned materials (Figure 7c, green color unit), similar to the Ph unit (*Chojnacki et al.*, 2010).

(2) low extended areas of bright-toned materials, corresponding to the bedrock, similar to the etched unit, associated with mid-toned materials in the ripple crests (Figure 7c, yellow color unit).

(3) high extended areas of bright-toned materials, corresponding to the bedrock, similar to the etched unit associated with mid-toned materials in the ripple crests (Figure 7c, orange color unit).

The in situ observations showed bright-toned outcrops from the Erebus Crater to the Endeavour crater (Figure 8a) which are associated with sulfate-rich bedrocks exposed in ripple troughs (Figure 8b, star 3). In the Botany Bay area, in situ observations showed flat polygonal fractured outcrops. The rocks are composed of layered features, with rounded coarse-grained materials (sand-sized particles), embedded in a matrix and cement, with a thin covering of soil (*Arvidson et al.*, 2014) (Figure 8b, star 4).

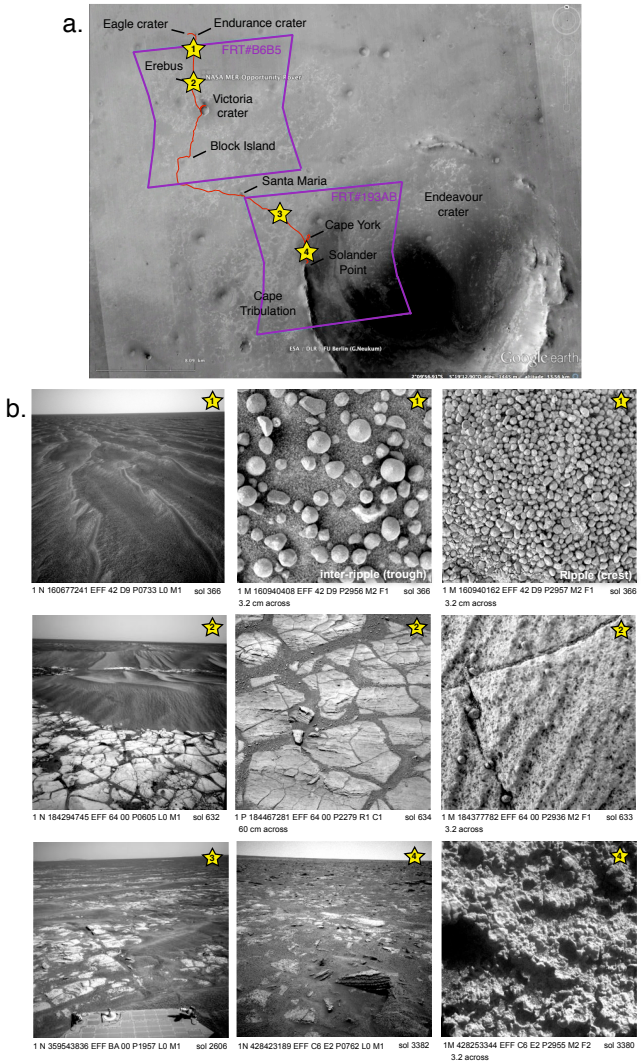

Figure 8: In situ observations from Navcam/MER (N), Pancam/MER (P) and MI/MER (M). (a) location of FRT#B6B5 (FRT#334D has the same footprint as FRT#B6B5) and FRT#193AB CRISM footprints (in purple color), the rover traverse (in red color) and the location of the selected in situ observations (star), (b) Navcam, Pancam and MI observations of the aeolian ripple region composed of hematitic concretions, basaltic sands and a small amount of dust (top row), Navcam, Pancam and MI observations of the aeolian ripple region with sulfate-rich outcrops at Erebus area (middle row) and Navcam and MI observations dark-toned sulfate-rich outcrops at Botany Bay at the west part of the Endeavour crater (bottom row).

3.2.3 Surface material photometric parameters

3.2.3.1. The single scattering albedo parameter

Figure 9c represents the map of the single scattering albedo values (ω). Spatial variations of the ω parameter are observed at 200m/pixel scale. In area 1, the regions mainly composed of dark-toned (Figure 7c, green color unit) and of mid-toned materials (Figure 7c, yellow color unit) are associated with the lowest ω values ($\omega_{CRISM} \leq 0.60$, $\sigma \leq 0.10$). The regions with a high proportion of bright-toned outcrops and accompanied with mid-toned materials (Figure 7c, orange color unit) are associated with the highest ω values ($\omega_{CRISM} \simeq 0.60 - 0.65$, $\sigma \leq 0.10$). In area 2, the crater floor composed of dark-toned material mantle (Figure 7c, green color unit) and the Botany Bay region (Figure 7c, blue color unit) are associated with the lowest ω values ($\omega_{CRISM} \simeq 0.40 - 0.50$, $\sigma \leq 0.10$). The bright-toned materials observed in the crater floor (Figure 7c, orange color unit) are associated with high ω, but lower than the bright-toned outcrops, observed in area 1 and in area 2 (Figure 7c, orange color unit) ($\omega_{CRISM} \simeq 0.60$, $\sigma \leq 0.10$).

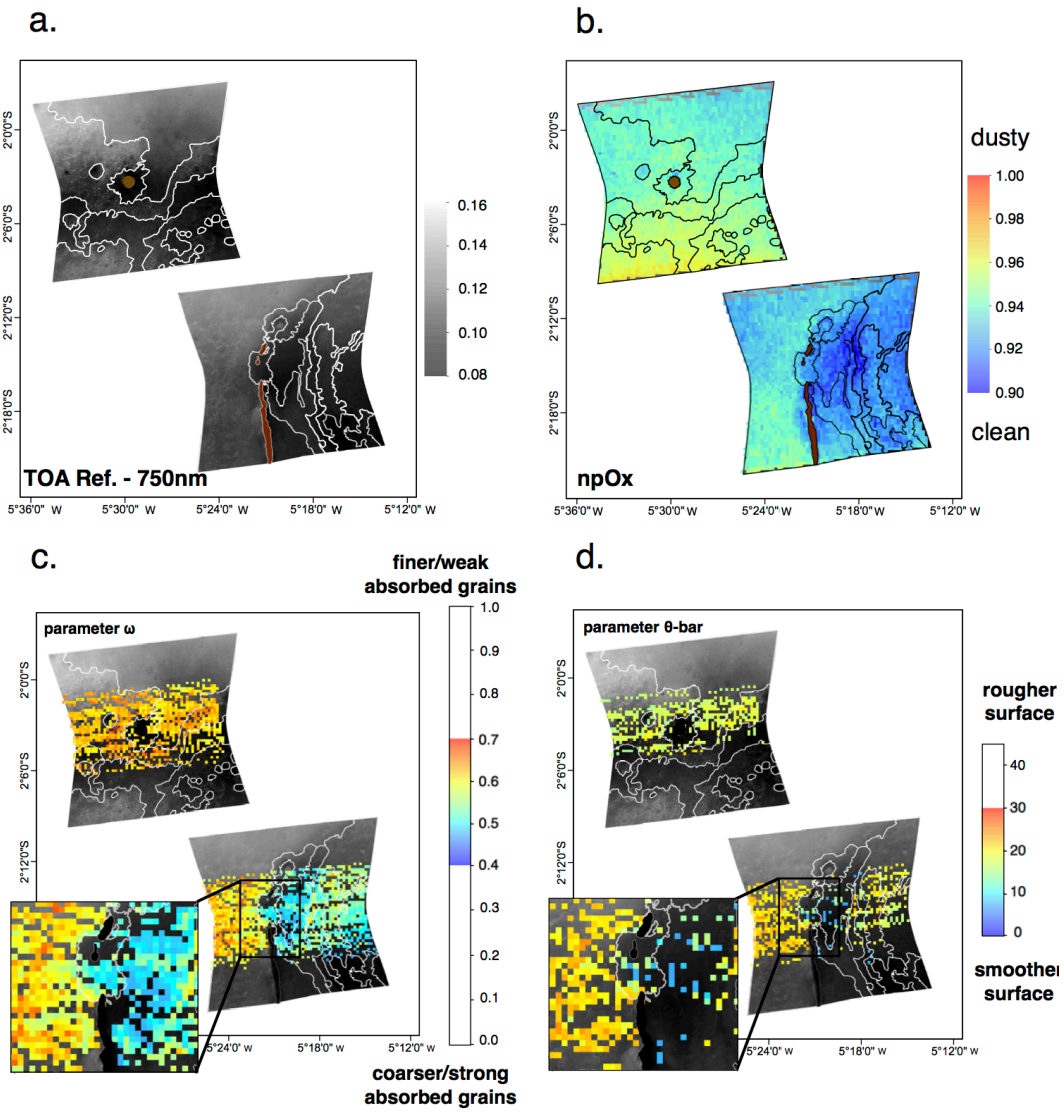

Figure 9: CRISM mapping of the combination of FRT#B6B5 - FRT#334D and FRT#193AB. a. TOA reflectance map in I/F unit at 20m/pixel at 750 nm. b. map of npOx spectral index (dust index) from FRT#B6B5 and from FRT#193AB at 200m/pixel. c. parameter ω map at 200m/pixel ($\sigma_\omega \leq 0.10$). d. parameter $\bar{\theta}$ map at 200/pixel ($\sigma_{\bar{\theta}} \leq 5°$). The colored pixels correspond to the value of the mean PDF at about 200m/pixel. Only the middle part of the central image is covered with all additional geometric images (up to 22 images for area 1 and up to 11 images for area 2) that it is why the photometric results are obtained in this area. Regions dominated by abrupt and high local topography (Victoria crater and Endeavour crater rim) are masked off in the photometric maps that would otherwise make the atmospheric correction and the photometric study more challenging (section 2.3).

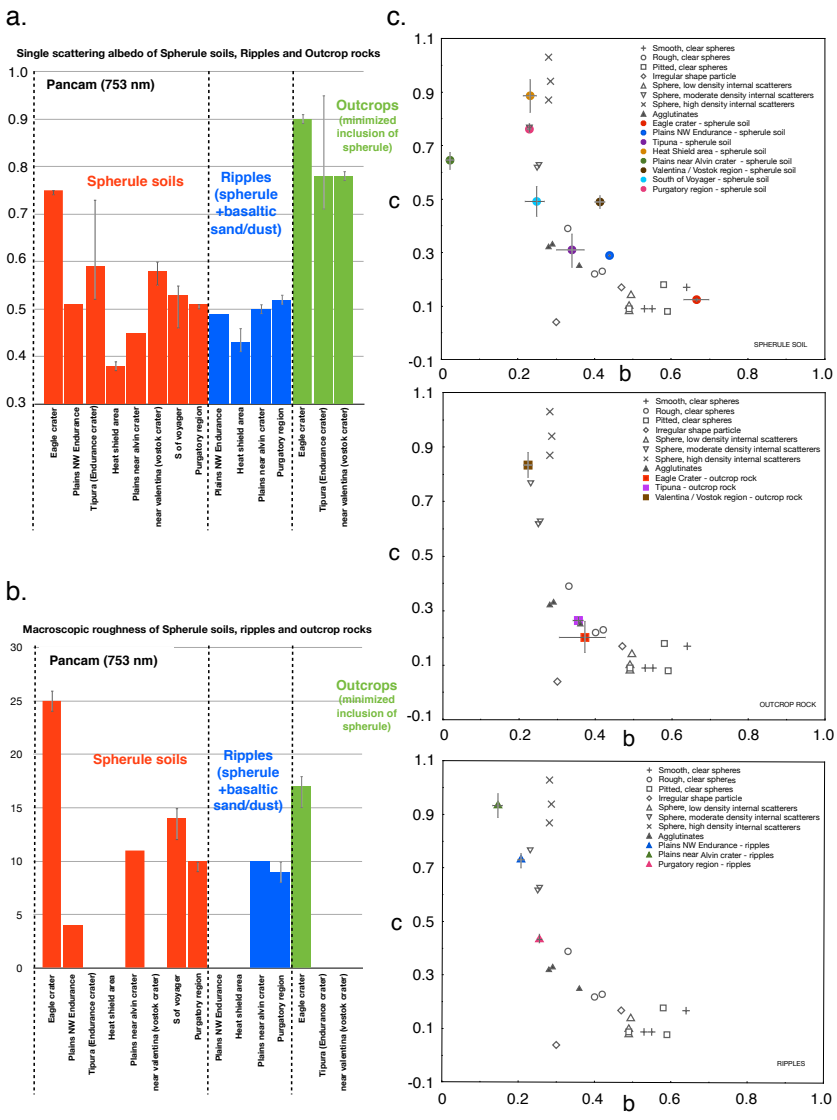

Figure 10: In situ photometric results from Pancam/MER: Mean and uncertainties of a. the single scattering albedo (ω), b. the macroscopic roughness ($\bar{\theta}$), c. the particle phase function parameters (b and c) overplot to the experimental b and c values pertaining to artificial particles measured by *McGuire and Hapke* (1995). All photometric parameters are estimated at 753 nm for different geological units at different sites along the traverse (from Sol 11 to Sol 473) (*Johnson et al.*, 2006b).

From orbital observations, four surface components are observed: (i) hematitic concretions, (ii) basaltic sands, (iii) dust and (iv) sulfate, consistent with the in situ observations. The optical constants (n, and k), at the studied wavelength (750 nm) shown in Table 3, are n=1.52, k=0.0011 for basalt (*Pollack et al.*, 1973), n=1.50, k=0.001 for dust (*Wolff et al.*, 2009), n=2.805, k=0.03478 (*Sokolik and Toon*, 1999) for hematite and n=1.5, k=0.00001 for sulfate (*Roush et al.*, 2007). Hematite has the highest k coefficient (leading to lowest ω) and the sulfate mineral the lowest (leading to highest ω). These are consistent with the CRISM ω results, where the lowest ω values are observed in aeolian ripples, mainly composed of hematitic concretions (Figure 7c, yellow and green color unit). The highest ω values are observed in regions associated with sulfate-rich bright-toned outcrops (Figure 7c, red and orange color units).

In situ images from Pancam and MI provide constraints on the particle size of each component, helpful for the ω values interpretation: (i) the basaltic granular materials are characterized by fine-grained sands with a mean size around 50 to 150 μm (*Herkenhoff, K. E., et al.*, 2006; *Herkenhoff et al.*, 2004b; *Weitz et al.*, 2006) (Figure 8b, top row), (ii) the hematitic concretions are characterized with a particle size around 1-2 mm (*Herkenhoff, K. E., et al.*, 2006; *Weitz et al.*, 2006; *Herkenhoff et al.*, 2004b) (Figure 8b, top row), (iii) the sulfate-rich bright-toned rocks are composed of moderate rounded well-sorted sand grains (from 0.2 to 1 mm) forming mm-scale laminations, fine-grained and coarser

cement crystals, cm-sized vugs, and 3- to 5-mm sized hematitic spherules embedded within the outcrops (*Herkenhoff, K. E., et al.*, 2006; *Squyres et al.*, 2004c) (Figure 8b, middle row), (iv) dust deposit of silt size (<4 μm in diameter) (*Lemmon et al.*, 2004) and (v) sulfate-rich dark-toned rocks composed of coarser grains (sand-sized) (*Arvidson et al.*, 2014) than the sulfate-rich bright-toned rocks (fine-sized). The coarse hematitic concretions (mm-sized) and the coarse grains in the sulfate-rich dark-toned rocks accentuates the decrease of ω values. The fine particles that compose the bright-toned outcrop and the dust cover in the plains accentuates the increase of ω values, consistent with the CRISM ω estimates.

For the hematite-rich concretions, the MI images did not show macroscopic evidence of internal structures within the $\sim$100 μm resolution of the instrument (*Herkenhoff et al.*, 2004b; *McLennan et al.*, 2005; *Herkenhoff et al.*, 2008). However, the emissivity measurements of the hematitic concretions from TES on-board MGS and Mini-TES on-board MER-Opportunity suggested that the emissivity is dominated by emission along the crystallographic c axis, explained by the lack of a 390 cm^{-1} feature in the hematite-rich spherule spectra (*Lane et al.*, 2002; *Glotch et al.*, 2004). To explain this observation, *Glotch et al.* (2006) from modeling and *Golden et al.* (2008) from experimental study suggested the presence of a high density of internal structure for the hematitic spherules (randomly oriented platy hematite crystal, concentric growth, or fibrous growth along the radial direction). For the sulfate-rich rocks, the MI images (Figure 8b) showed macroscopic evidence of heterogeneity in the sedimentary rocks with the presence of fine-grained and coarser cement crystals. For the basaltic granular medium, the MI resolution did not show evidence of an internal structure within the $\sim$100 μm resolution of the instrument. However, the basaltic grains are generally composed of particles with high internal structures, such as minerals or bubbles, similar to the Gusev basaltic sands. For the three components (hematitic concretions, sulfate-rich rocks and basalt), the ω values may be higher than their counterpart (those with no internal structures), consistent with the CRISM ω estimates.

The single scattering albedo values, estimated by CRISM, are compared to those estimated from Pancam measurements (*Johnson et al.*, 2006b) (Figure 10a). Indeed, the in situ instruments can distinguish rocks and soils whereas CRISM observes an extended area including rocks and soils (unit mixtures). Pancam measurements were taken at 753 nm for different geological units (rocks and soils) (*Johnson et al.*, 2006b): (i) the Outcrop unit refers to as the sulfate-rich bedrock, (ii) the Spherule soil unit refers to as unconsolidated materials of basaltic sands and of hematitic concretions, and (iii) the Ripple soil unit refers to as the ripple crest materials composed of basaltic sands, hematitic concretions and a small amount of dust (the population of hematitic concretions is greater than the Spherule soil unit). The Outcrop unit showed the highest ω values ($\omega_{Pancam} < 0.90$). For the Ripple soil and Spherule soil units, the lowest ω values were modeled ($\omega_{Pancam} < 0.60$) (Figure 10a). However, the Ripple soils unit showed lower ω values ($\omega_{Pancam} < 0.50$) than the Spherule soils ($\omega_{Pancam} < 0.60$)(Figure 10a). This discrepancy can be explained by the higher abundance of hematitic concretions in the ripple crests (accumulation during the wind transport) compared the ripple troughs and the soils (*Herkenhoff et al.*, 2004b; *Herkenhoff, K. E., et al.*, 2006; *Weitz et al.*, 2006) (Figure 8b, top row). The direct comparison of the CRISM results to those estimated from in situ Pancam measurements is presented below.

(1) The regions mainly composed of mid-toned materials in areas 1 and 2 (Figure 7c, yellow color unit) show consistent values ($\omega_{CRISM} \leq 0.60$, $\sigma \leq 0.10$) with the Pancam estimates, obtained for the Spherule soil and Ripple soil units ($\omega_{Pancam} < 0.60$).

(2) The regions with a high proportion of bright-toned outcrops and accompanied with mid-toned materials in areas 1 and 2 (Figure 7c, orange color unit) show lower values ($\omega_{CRISM} \simeq 0.60 - 0.70$, $\sigma \leq 0.10$) than the Pancam estimates ($\omega_{Pancam} \simeq 0.9$), which can be explained by the spatial resolution difference between Pancam and CRISM. Indeed, Pancam distinguishes individual units of rock (e.g., Outcrop unit) and soil (e.g., Spherule soil and Ripple soil) whereas CRISM measures areas integrating different geological units. A mixture of Spherule soils or Ripple soil units, characterized by lower ω values ($\omega_{Pancam} < 0.6$), with the Outcrop unit, characterized by higher ω values ($0.77 < \omega_{Pancam} < 0.90$), seems to slightly decrease the ω values, consistent with the lower ω values obtained from CRISM observation. In their experimental studies, *Johnson et al.* (2013) showed that the addition of 2-3 mm- sized spherules with thin hematite rims, on an analog of the sulfate-rich sedimentary rocks, composed of finer particles, decrease the ω values. The influence of mixtures in the scattering behavior between hematitic concretions and basalt and between hematitic concretions and sulfate are tested by a numerical modeling in Subsection 4.2.

(3) The regions including the Botany Bay area, composed of dark-toned sulfate-rich outcrops (Figure 7c, blue color unit), show lower values ($\omega_{CRISM} \simeq 0.45 - 0.50$, $\sigma \leq 0.10$) than those estimated for the Outcrops unit by Pancam ($0.77 < \omega_{Pancam} < 0.9$). This suggests that there is a difference in the physical properties. Coarser grains can explain the low ω values in the dark-toned outcrops regions, confirmed by the in situ observations (*Arvidson et al.*, 2014) as could the prevalence of dark-toned basaltic grains and coatings interspersed with the outcrop materials within the Botany Bay area.

(4) The regions composed of a dark-toned mantle in the Endeavour crater floor (Figure 7c, green color unit in area 2) show lower values ($\omega_{CRISM} \simeq 0.40 - 0.50$, $\sigma \leq 0.10$) than those estimated from the Spherule soil and Ripple soil units ($\omega_{Pancam} < 0.60$) and than those estimated at the region around Victoria Crater (Figure 7c, green color unit in area 1). Lower values are also observed compared to the region of aeolian ripples without sulfate-rich outcrops (Figure 7c, in

yellow color unit). The npOx index value (Figure 9b) indicates that the surface is less contaminated by dust, compared to all units in area 1. As observed at MER-Spirit landing site (Subsection 3.1.3), dust is characterized by high ω values ($\omega_{CRISM} \sim 0.80$). Consequently, its relative paucity in the crater floor is consistent with the lower mean ω values.

3.2.3.2. The particle phase function parameters

Figures 11a and 11b present the asymmetry parameter (b) and the backscattering fraction (c) respectively. At first order, the surface material is characterized by a broad backscattering behavior ($c > 0.5$ and $b < 0.5$ similar to particles with moderate density of internal scatterers (Figure 11c)). Moreover, we note that the c values are slightly higher in area 2 than in the area 1 (Figure 11b).

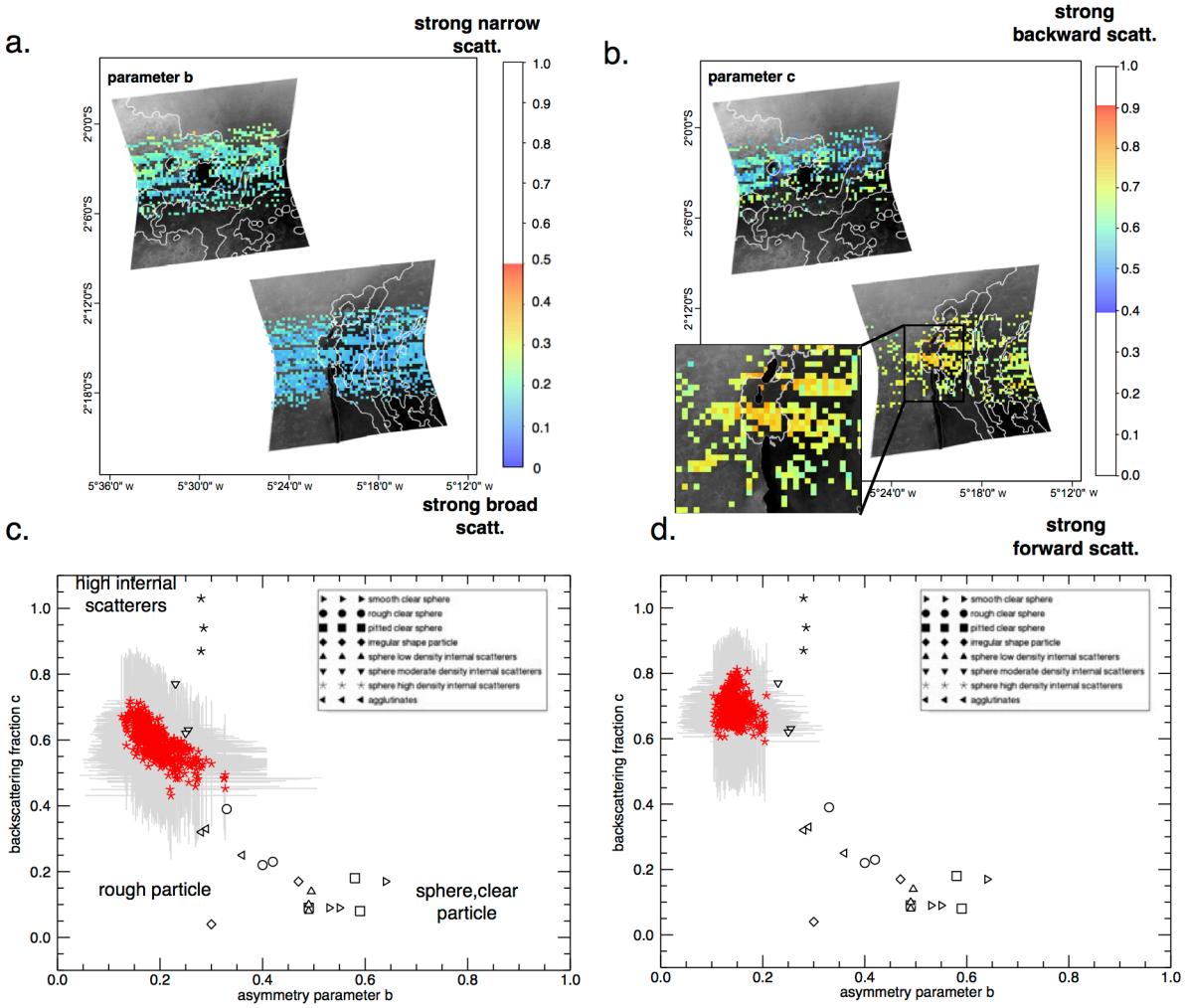

Figure 11: CRISM mapping of the combination of FRT#B6B5 - FRT#334D and FRT#193AB. a. parameter b map at 200m/pixel ($\sigma_b \leq 0.20$). b. parameter c map at 200m/pixel ($\sigma_c \leq 0.20$). The colored pixels correspond to the value of the mean PDF at about 200m/pixel. Only the middle part of the central image is covered with all additional geometric images (up to 22 images for area 1 and up to 11 images for area 2) that it is why the photometric results are obtained in this area. c. and d. graph of the asymmetry parameter (b) versus backscattering fraction (c) estimated from FRT#B6B5 - FRT#334D (Figure 11c) and from FRT#193AB (Figure 11d) plotted with experimental values on artificial particles from *McGuire and Hapke* (1995).

.

The particle phase function parameters estimated by CRISM are compared to those estimated from Pancam measurements at 753 nm (*Johnson et al.*, 2006b) (Figure 10c) to understand the mean surface scattering behavior.

(1) The crater floor composed of dark-toned material mantle (Figure 7c, green color unit in area 2) shows the highest c values ($c_{CRISM} \sim 0.75 - 0.80$, $\sigma \leq 0.20$). Values are consistent with those estimated for Spherule soil and Ripple soil units

(Figure 10c). As discussed previously, the b and c values are consistent with the presence of an internal structure in the hematitic concretions, determined from Mini-TES spectra. Moreover, the b and c values are consistent with the physical properties of typical basaltic materials, composed of high internal structure such as the basaltic sands at MER-Spirit area (Subsection 3.1.3).

(2) The dark-toned sulfate-rich bedrocks (e.g., Botany Bay) (Figure 7c, blue color unit in area 2) show the highest c values ($c_{CRISM} \sim 0.75-0.80$, $\sigma \leq 0.20$). We note a difference in the c values compared to aeolian ripples with sulfate-rich outcrops (Figure 7c orange and red color units), that suggests a difference in physical properties. The high c values can be explained by the presence of greater heterogeneity inside the outcrops, compared to the bright-toned outcrops. This is consistent with the in situ observations which showed that the dark-toned sulfate rocks are composed of coarser grains (sand-sized grains), embedded in a matrix and cement (*Arvidson et al.*, 2014)).

(3) The regions mainly composed of mid-toned materials (Figure 7c, yellow color unit in areas 1 and 2), show intermediate c values ($c_{CRISM} \sim 0.60 - 0.75$, $\sigma \leq 0.20$). Values are consistent with those estimated for the Spherule soil and Ripple soil units from Pancam, (Figure 10c). Lower c values are obtained, compared to the dark-toned mantle at Endeavour crater floor (Figure 7c, green color unit). Again, this difference can be explained by the presence of small amount of dust in the aeolian ripples of dark-toned materials (the npOx index is close to 0.94, Figure 9b). *Johnson et al.* (2006c) showed a more forward scattering behavior for isolated dust particles, consistent with the scattering behavior of typical atmospheric dust particles, as modeled by *Tomasko et al.* (1999) and *Lemmon et al.* (2004), over the Mars Pathfinder and MER landing sites. The mixture of dust with the unconsolidated materials of hematitic concretions and basaltic sands can explain the decrease of c values.

(4) The regions with a high proportion of bright-toned outcrops and accompanied with mid-toned materials in area 1 (Figure 7c, orange color unit) show the lowest c values ($c_{CRISM} \sim 0.50 - 0.60$, $\sigma \leq 0.20$) and lower c values than the equivalent unit in area 2 ($c_{CRISM} \sim 0.70 - 0.75$, $\sigma \leq 0.20$). Compared to the in situ photometric results from Pancam measurements (*Johnson et al.*, 2006b), higher c values are observed than those estimated from Pancam for typical Outcrop units in Eagle crater and Tipuna (Figure 10c). This difference can be explained by the difference of the spatial resolution and sampling strategy used for the different geological units. Whereas CRISM pixels integrate over several geological units (basaltic granular materials, hematitic concretions, dust and sulfate-rich outcrops), Pancam data were extracted from individual portions of Outcrop blocks, typically without significant surface relief (*Johnson et al.*, 2014). The MI images of the sulfate-rich outcrops (Figure 8b) showed evidence of heterogeneity in the sedimentary rocks which creates high scattering, consistent with a high c value.

3.2.3.3. The surface macroscopic roughness parameter

Figure 9d represents the map of the surface macroscopic roughness parameter ($\bar{\theta}$) values. We observe high $\bar{\theta}$ values (∼15-25°), higher than those estimated at Gusev plain. We note that: (i) the region with a high extended area of bright-toned outcrops and accompanied with mid-toned materials (Figure 7c, orange color unit) and the region mainly composed of mid-toned materials (Figure 7c, yellow color unit) are associated with the highest $\bar{\theta}$ values ($\bar{\theta}_{CRISM} \simeq$ 15-25°, $\sigma \leq 5°$, Figure 9d), (ii) the Botany Bay region, composed of dark-toned outcrops (Figure 7c blue color unit) and the dark-toned material mantle in the crater floor in area 2 (Figure 7c, green color unit) show the lowest $\bar{\theta}$ values ($\bar{\theta}_{CRISM} \simeq 5°$, $\sigma \leq 5°$, Figure 9d).

To examine the high $\bar{\theta}$ values, the mean slope is calculated from HiRISE DTM, available in the area 2 at scale of 1 meter per pixel (Figure 7c). By comparing the $\bar{\theta}$ parameter map to the mean slope, the high $\bar{\theta}$ values are not correlated with a high mean slope and confirm again that the macroscopic roughness parameter is more sensitive to the microscopic topography (from the particle to a few mm).

The macroscopic roughness values estimated by CRISM are comparable to those estimated from Pancam measurements at 753 nm (*Johnson et al.*, 2006b) (Figure 10b).

(1) The regions mainly composed of mid-toned materials (Figure 7c, yellow color unit) show higher $\bar{\theta}$ values ($\bar{\theta}_{CRISM} \simeq$ 15-25°) than in situ photometric results (Figure 10b) for Spherule soil and Ripple soil units ($\bar{\theta}$ averages of ∼13±7 and ∼10±1 °, respectively). In situ observations showed that most of Meridiani soils (in plains and the ripple troughs which are the most sampled in a CRISM pixel) are composed of spaced millimeter-sized hematite spherules above a sand-sized basalt deposit (Figure 8b, top row), as represented in Figure 12, case 2. This particle distribution creates a high shadow hiding which explains the high $\bar{\theta}$ values of the CRISM and Pancam results. *Johnson et al.* (2013) showed in their experimental studies on Mars analog materials that the addition of spherules <2-3 mm in diameter with thin hematite rims, on an analog of the spherule-bearing sulfate sedimentary rock much finer particles (silt/sand size), caused the increase of the $\bar{\theta}$ values (from 7° to 26°). Those results are consistent with those observations. Moreover, we can notice slightly higher $\bar{\theta}$ values for the Spherule soils unit than for the Ripple soils unit that can be explained by higher area density of spherules in the Ripple units (Figure 8b, top row) on average. Consequently, the high average CRISM $\bar{\theta}$ estimates, compared to those

derived from Pancam measurements can be explained by a more extended sampling of the Spherule soils unit. Indeed, Spherule soils unit represents the most extended unit in the landscape, compared to the Ripple unit (Figure 8b, top row).

(2) The regions with a high extended area of bright-toned outcrops and accompanied with mid-toned materials (Figure 7c, orange color unit) show consistent $\bar{\theta}$ values with the in situ photometric results (Figure 10b) for Outcrop units ($\bar{\theta}$ =15-20°). Again, the presence of small population of hematitic concretions on the sulfate-rich outcrops can create high shadow hidings which can explain the high $\bar{\theta}$ values, as shown in Figure 12, case 4. Moreover, in situ observations showed that the sulfate-rich outcrops are highly textured (broad and weakly filled by hematite-rich spherules) which creates a high local slope. This high local slope can explain the high $\bar{\theta}$ values (Figure 12, case 4). Furthermore, high $\bar{\theta}$ values are noticed in the aeolian ripples with sulfate-rich outcrops in area 2, compared to those in the area 1 (Figure 7c, in orange color unit). This can be explained by higher exposure of sulfate-rich outcrops in area 2, due to the removal of superficial dust, also observed in the npOx map (Figure 9b). The TI values estimated from THEMIS measurements are higher in the aeolian ripples with sulfate-rich outcrops in the area 2 (THEMIS TI values: ∼155-180 $J.m^{-2}.K^{-1}.s^{-1/2}$ (*Arvidson et al.*, 2011)) than those observed in the area 1 (THEMIS TI values: ∼140 -145 $J.m^{-2}.K^{-1}.s^{-1/2}$ (*Arvidson et al.*, 2011)), consistent with the $\bar{\theta}$ values. Those observations are consistent with our results.

(3) The region composed of dark-toned sulfate rich outcrop (Botany Bay) (Figure 7c, blue color unit) shows the lowest $\bar{\theta}$ values ($\bar{\theta} \sim 5°$, $\sigma \leq 5°$, Figure 9d). The $\bar{\theta}$ values can be explained by (i) small population of hematite-rich spherules atop the outcrops, and/or (ii) small population of desiccated features or narrower and/or (iii) the latter are filled by hematite-rich spherules which create a smooth area (Figure 12, case 5).

(4) The dark-toned material mantle (hematite-rich spherules and basaltic sand-sized grains) in the crater floor (Figure 7c, green color unit in area 2) shows the lowest $\bar{\theta}$ values ($\bar{\theta} \sim 5°$, $\sigma \leq 5$ °, Figure 9d). In situ observations are not available in this area, but we suggest that the low $\bar{\theta}$ values can be the result of: (i) the high density of hematitic concretions disposed nearby, if hematite-rich spherules cover the basaltic medium (Figure 12, case 1), or (ii) if hematite-rich spherules are absent, the presence of basaltic fine-grained materials creating a smooth surface (Figure 12, case 3).

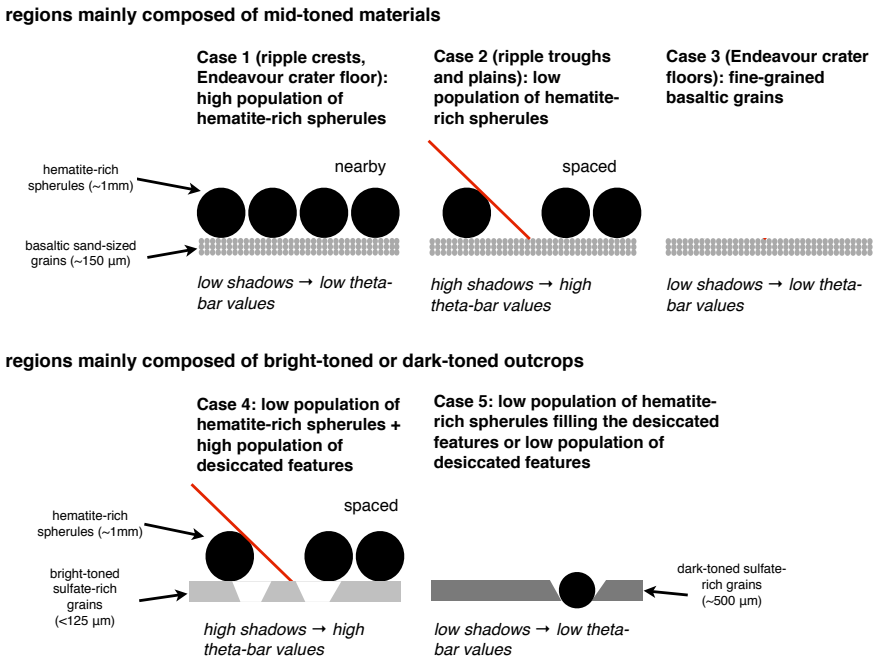
regions mainly composed of mid-toned materials
Case 1 (ripple crests, Endeavour crater floor): high population of hematite-rich spherules
Case 2 (ripple troughs and plains): low population of hematite-rich spherules
Case 3 (Endeavour crater floors): fine-grained basaltic grains
hematite-rich spherules (~1mm)
basaltic sand-sized grains (~150 µm)
nearby
spaced
low shadows → low theta-bar values
high shadows → high theta-bar values
low shadows → low theta-bar values
regions mainly composed of bright-toned or dark-toned outcrops
Case 4: low population of hematite-rich spherules + high population of desiccated features
Case 5: low population of hematite-rich spherules filling the desiccated features or low population of desiccated features
hematite-rich spherules (~1mm)
bright-toned sulfate-rich grains (<125 µm)
spaced
dark-toned sulfate-rich grains (~500 µm)
high shadows → high theta-bar values
low shadows → low theta-bar values

Figure 12: Schematic representation of the meaning of the macroscopic roughness values and the relation to the surface roughness in Meridiani Planum in regions dominated by dark-toned materials and bright-toned or dark-toned outcrops.

4 Modeling

In the Section 3, photometric results were obtained in the MER landing site regions and discussed by comparing the in situ and orbital observations. However, several questions remain. Indeed, we observed from the in situ images that the surface is mainly composed of material mixtures. Consequently, it is important to know what kind of particles can control the overall photometric behaviors in a mixture and how we can relate the photometric results to the surface mixtures. Moreover, the information about the particle internal structure, derived from the single scattering albedo and

phase function parameters, can be useful to constrain the geological processes (e.g., the presence or the absence of an internal structure in an igneous material can inform us about the crystallization mode).

The radiative transfer model and analytic approaches are helpful to analyze the remote sensing measurements, to relate them in terms of surface material properties, and to reproduce realistic situations allowing us for a better understanding of the physical properties.

To better understand the relation between the single scattering albedo parameter and the microscopic properties of the particles such as the composition (complex indices of refraction), the particle diameter (path length) and on the particle internal structure (density of internal scatterers), we used an analytic approach. In radiative transfer modeling, little is known about the range of internal scatterers coefficient (s) (see subsection 4.1 and the Appendix A) values and they are usually set to 0 for simplification (e.g., *Lucey*, 2000). Similarly, the relation between this coefficient and the internal structure of a particle is underconstrained (e.g., *Hapke*, 2012b). Here, we estimated the internal scatterers coefficients of the observed compounds, at both MER landing sites by using a combination of the CRISM single scattering albedo values (Section 3) and the in situ information in Section 4.1.

Most commonly planetary surfaces are composed of a mixture of different materials. Consequently, the reflected radiation measurements from the CRISM instrument (spatial resolution: 200m/pixel) is a signal from different components of the surface. Moreover, little is known on what controls the overall photometric behavior of a mixture (e.g., spatial, intimate, stratified) made of different material properties. To understand the meaning of each photometric parameter estimated from CRISM observations and to evaluate which compound controls the overall photometric behavior, we performed realistic simulations by mimicking, as possible, the mixtures observed in the MER landing sites in Subsection 4.2.

4.1 Density of internal scatterers

The theoretical formulation of Hapke (eq. 6.47-6.50, *Hapke* (2012a), Appendix A) is used to relate the single scattering albedo (ω) to the microscopic properties of particles, including the complex indices of refraction (n and k) related to the particle composition, the path length (D) related to the particle size, the internal scattering coefficient (s) and the density of internal scatterers (sD) related to the particle internal structure. This formulation is used here for the calculation of the single scattering albedo value, knowing the particle properties.

For the case of MER-Spirit landing site, the ω values of basalt and nanophase ferric oxide dust are calculated from the optical constants, detailed in Table 3. First, the ω value is calculated for typical dust, assuming isolated atmospheric particles with a diameter 3 μm and no internal structure ($s = 0$) (*Lemmon et al.*, 2004). This ω value is around 0.9 (Figure 13), which is higher than the ω values estimated from CRISM observations in the dustier area in Figure 3b ($\omega_{CRISM} \sim 0.80$). The lower ω_{CRISM} value can be explained by aggregated dust with greater effective particle size. The ω value calculated for coarser dust with a diameter 10 μm as a function of the density of internal scatterers (sD) is shown in Figure 13. To have similar single scattering albedo values as the CRISM estimates ($\omega_{CRISM} \sim 0.80$), internal scatterers must be included ($s = 3.8\,\mu m^{-1}$ equivalent to $sD \sim 40$). This result is consistent with the in situ observations showing that dust is aggregates of unresolved subparticles (*Herkenhoff et al.*, 2004a; *Sullivan et al.*, 2008; *Vaughan et al.*, 2010). Second, the ω value is calculated for typical basalt ($\simeq 500$ μm, Subsection 3.1.3, (*Herkenhoff et al.*, 2004a; *Herkenhoff, K. E., et al.*, 2006)) for different values of s parameter. To have similar single scattering albedo values as the CRISM estimates of the regions where the basaltic medium (less contaminated by dust) is visible in Figure 3b ($\omega_{CRISM} \sim 0.55$), $s = 0.68\,\mu m^{-1}$ equivalent to $sD \sim 300$, must be used, consistent with the high CRISM c parameter values.

For the case of MER-Opportunity landing site, the ω values of hematite and sulfate are calculated from the optical constants and particle size, detailed in Table 3. Because the MI spatial resolution is limited to $\sim$100 μm resolution, the component size of sulfate-rich outcrops is unknown. Consequently, we decided to refer to the *Johnson et al.* (2013)'s experimental works. They selected a hematite–siderite spherule-bearing paleosol as an analog to the spherule-bearing sulfate-rich sedimentary rocks formed of a matrix soil of < 45 μm particles. For a typical sulfate grain size ($\simeq 40$ μm) and hematite grain size ($\simeq 1000$ μm) (because the hematite proportion in the spherules is unknown, we suppose that all the spherule is composed of hematite in first order), we note that the introduction of internal scatterers (sD) does not significantly change the ω value, compared to basalt and dust (Figure 13). This is due to the fact that sulfate is very bright, and that hematite has a very large grain size, and their physical properties take precedence over the density of internal scatterers.

Site	Material	n	k	s (μm^{-1})	D (μm)	b	c
Spirit	dust	1.5 (*Wolff et al.*, 2009)	0.001 (*Wolff et al.*, 2009)	3.8 (Subsection 4.1)	10 (*Lemmon et al.*, 2004)	0.3	0.6[1] (*Johnson et al.*, 2006a)
	basalt	1.52 (*Pollack et al.*, 1973)	0.0011 (*Pollack et al.*, 1973)	0.68 (Subsection 4.1)	500 (*Herkenhoff, K. E., et al.*, 2006)	0.3	0.8 (Subsection 3.1.3)
Opportunity	hematite	2.805 (*Sokolik and Toon*, 1999)	0.03 (*Sokolik and Toon*, 1999)	0 (Subsection 4.1)	1000 (e.g., *Herkenhoff et al.*, 2008)	0.3	1.0 (Subsection 3.2.3)
	basalt	1.52 (*Pollack et al.*, 1973)	0.0011 (*Pollack et al.*, 1973)	0.68 (Subsection 4.1)	150 (e.g., *Herkenhoff et al.*, 2008)	0.3	0.8[3] (Subsection 3.1.3)
	sulfate	1.5 (*Roush et al.*, 2007)	10^{-5} (*Roush et al.*, 2007)	0 (Subsection 4.1)	40(*Johnson et al.*, 2013)	0.3	0.2[2] (*Johnson et al.*, 2013)

n: refractive index, k: absorption coefficient, s: internal scattering coefficient, D: path length related to the particle size, b: the asymmetry parameter from the two-term Henyey Greenstein function, c: backscattering fraction from the two-term Henyey Greenstein function
[1]similar to the scattering properties of Bright soil unit of the Landing site obtained from Pancam (*Johnson et al.*, 2006a), corresponding to the most dustier area).
[2]based on *Johnson et al.* (2013)'s experimental photometric results on an analog to the spherule-bearing sulfate sedimentary rocks observed at MER-Opportunity landing site
[3]same b and c values estimated for the basaltic granular medium for the case of Gusev crater

Table 3: Physical parameters at 750 nm used for the calculation of the s parameter in Section 4.1 and for the mixture simulations in Section 4.2. The justifications are discussed in the text in Section 4.2.

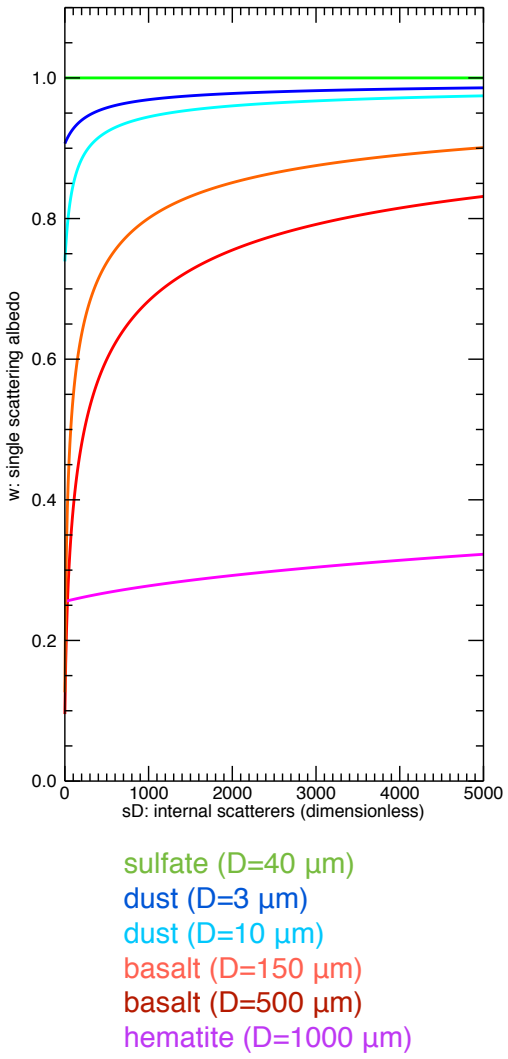

Figure 13: Graph of the calculated single scattering albedo (ω) from the *Hapke* (2012b) formulation (eq. 6.47-6.50, Appendix A) as a function of the internal scattering coefficent (sD) for the typical particle size of basalt (500 μm, in dark red color), of dust (3 μm, in dark blue color and 10 μm, in light blue color), of hematite (1000 μm, in purple color) and of sulfate (40 μm, in green color).

4.2 Mixtures

In natural environments, planetary surfaces are composed of a mixture of different materials (e.g., with different grain size, composition, internal structure). For instance, at the selected areas at the MER landing sites, several kind of mixtures are observed: dust deposits on basaltic unconsolidated materials observed at the MER-Spirit landing site and lags of hematite concretions on basaltic unconsolidated materials observed at the MER-Opportunity landing site.

However, little is known about the influence of each compound of the mixture on the reflected radiation and more specially on the overall phase curve. By using a new radiative transfer model (*Pilorget et al.*, 2013), *Pilorget et al.* (2015) studied the evolution of the phase curve for various kinds of mixtures (spatial, intimate, and layered). The authors noticed that the phase curve evolution is controlled by the most abundant / brightest / highly anisotropic scattering grains within the mixture. The spatial and intimate mixtures showed similar trends in the phase curves when the grain properties varied. For the case of layered mixtures, the overall phase curves were generally very sensitive to the grain properties of the top layer.

In order to interpret our photometric results at the MER landing sites, we performed realistic simulations by attempting to mimic the observed mixtures. For that purpose, we used the same radiative transfer model as for the *Pilorget et al.* (2015)'s work (*Pilorget et al.*, 2013) which simulates light scattering in compact granular media using a Monte-Carlo

approach. The physical and compositional properties can be specified at the grain scale, allowing different kinds of mixtures (spatial, intimate and stratified). The radiative transfer is calculated by using a ray tracing approach between the grains and probabilistic physical parameters, such as a single scattering albedo and a phase function, at the grain scale. The single scattering albedo is calculated using the *Hapke* (1993, 2012a) formulation (Appendix A) and, thus is a function of the complex optical index of the material, the grain size and the potential inclusion of internal scatterers. A two-lobe Henyey-Greenstein phase function is also used in the model, consistent with the method described in the previous sections.

The photons' wavelength is 750 nm and their incidence angle is set at 45°. A porosity of 0.5 is assumed. The reflectance factor is computed in the -80, +80° emergence range. These results are then inverted by comparing and fitting the phase curves with the ones of homogeneous samples with various single scattering albedos and phase functions. Uncertainties are estimated to be within the ± 0.01 range for the parameter c and ± 0.02 for the parameter ω.

In the MER-Spirit landing site at Gusev Crater, dust may cover a surface made of basalt grains or even fill the space pores between them in regions affected by dust devils (Figures 14).

In the MER-Opportunity landing site at Meridiani Planum, hematitic concretions may cover the surface composed of basaltic grains or composed of sulfate-rich outcrops (Figure 15).

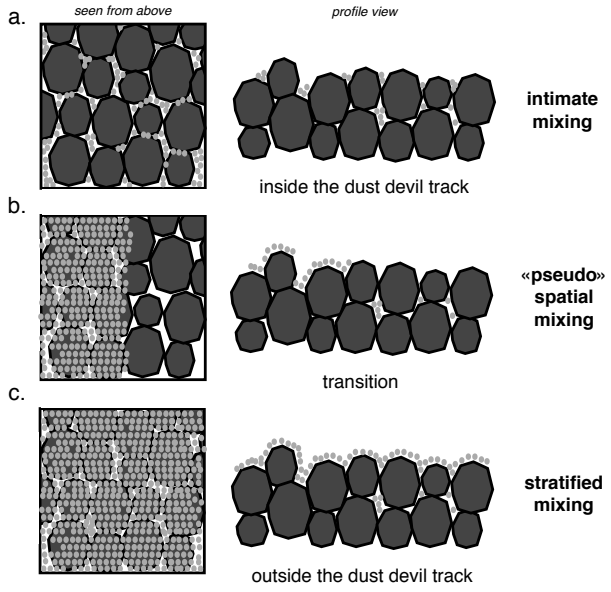

Figure 14: Schematic representation (seen from above and profile view) of different mixtures tested with the numerical model for the case of MER-Spirit area (not at scale): (a) the intimate mixture observed inside a dust devil track, (b) "pseudo" spatial mixture in dust devil track transition, (c) the stratified mixture observed outside a dust devil track. The particle sizes used here are: 500 μm for basaltic grains and 10 μm for dust (assumed as a clumping of small dust).

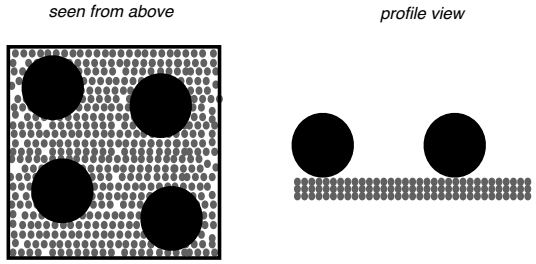

Figure 15: Schematic representation (seen from above and profile view) of mixtures tested with the numerical model for the case of MER-Opportunity area (not at scale): hematitic concretions (coarse black grains) on basalt or on sulfate layers (finer grey grains).The particle sizes used here are: 1000 μm for concretions, 500 μm for basaltic grains and 40 $\mu m$for sulfate grains.

For the simulations, several parameters must be known for each component of the mixture, but little is known about

their complex indices of refraction, internal structure, shape and roughness. We decided to choose the following values:

(1) The composition, described by the complex indices of refraction (n and k), can be estimated from analogous samples from laboratory measurements (e.g., for basaltic, hematite, sulfate materials) or from spaceborne observations (e.g., for dust). We assumed the hematite fraction in the concretions was 100%.

(2) The density of internal scatterers (noted s) is generally unknown for any samples (e.g., *Lucey*, 2000). This parameter was evaluated in Subsection 4.1.

(3) The particle size (noted D) can be evaluated from in situ observations from the MI instruments (e.g., for basaltic and hematite materials) as long as the particle size is greater than the spatial resolution of the instrument. For instance, the dust and sulfate grain sizes are unknown. The dust in Gusev Crater was observed as a clumping of individual dust grains forming coarse aggregates in local areas along the rover traverse ($\leq$150 μm) (*Sullivan et al.*, 2008; *Vaughan et al.*, 2010). However, due to the spatial resolution limitation of the MI instrument, smaller aggregates may exist. We decided to simulate with a mean value of dust aggregates set at 10 μm. For the sulfate grains, we decided to choose the similar particle size used in the *Johnson et al.* (2013)'s experimental work on analogous samples (40 μm). In their study, the authors showed similar photometric results with those from in situ measurements.

(4) The particle phase function of each compound is unknown. For the Gusev crater case, the parameters b and c of dust are similar to the scattering properties of Bright soil unit of the Landing site obtained from Pancam (*Johnson et al.*, 2006a), corresponding to the most dusty area. For the basaltic grains, the phase function parameters b and c are the same as those estimated for the basaltic granular medium for the case of Gusev crater from CRISM data, corresponding to values less influenced by dust, compared to the in situ measurements where the media are usually covered by a thin dust layer (*Johnson et al.*, 2006a). For the Meridiani Planum case, the parameters b and c of sulfate material are those estimated by *Johnson et al.* (2013). The phase function parameters b and c for the basaltic sands are assumed to be same as those at the Gusev Crater plain. For the hematite-rich spherules, as discussed previously, the concretions may be composed of internal structures, such as an internal growth (concentric or radial) (*Glotch et al.*, 2006; *Golden et al.*, 2008), creating a high density of internal scatterers. The associated scattering behavior is therefore assumed broad and backscattered.

All the cases are simulated using the input parameter values summarized in Table 3.

Figure 16 represents the simulation for Gusev Crater showing the evolution of the single scattering albedo (Figure 16a) and the backscattering fraction parameter (Figure 16b) (the parameter b is constant), when dust is added to a soil composed of basaltic sands. Dust is modeled as 10 μm agglomerates of smaller dust particles and each agglomerate is modeled as a discrete solid volume with the parameters b and c as measured at insitu (*Johnson et al.*, 2006a) ($b = 0.3$, $c = 0.6$ and $s = 3.8$, Table 3). Both intimate (Figure 14a) (in red in Figure 16) mixture and partial blanket case (Figure 14c) (in blue in Figure 16) are tested. For the intimate case, dust agglomerates are set between the basaltic grains like in Figure 14a. For the layered case, dust agglomerates are set as a layer of a unique agglomerate, representing a 10 μm thickness dust layer on top of the basaltic granular medium. In the simulations, a contiguous areal fraction (from 0 to 100%) of the basaltic granular medium is covered by the dust (Figures 14b and c).

Simulations show that when dust is situated within the space pores (intimate case), only a small volume fraction is sufficient to hide the photometric response of the basaltic granular medium (Figures 14c, 16). When covering the basaltic granular medium by dust grains, the evolution of parameters ω and c tends to be linear as the areal fraction covered by dust increased, which is consistent with some kind of checkboard mixture.

Modeling results also show that a 10 μm thick layer of dust has a strong impact on the photometric response of the underlying basaltic medium (Figures 14c, 16). When dust covers 100% of the basaltic granular medium, the influence of basaltic grains is small, but still exists, since voids are present between the dust grains. Such results, however, depend on both porosity and the geometric configuration of the grains. A higher porosity, as could be the case in agglomerates, will tend to increase the influence of the underlying substrate (*Pilorget et al.*, 2015). With 5% of dust in volume fraction, the parameter ω of the mixture is $\sim$0.7 and the parameter c is $\sim$0.69. We obtained similar values for the layered case when 70% of surface area is covered by a 10 μm thick layer of dust (Figure 16).

These results show that in the Gusev crater area, the presence of dust (layer or in the space pores) drives the mean scattering behavior and can mask the underlying material and the variability of scattering properties of materials. The dust devils are not sufficient to remove all dust (layer or in the space pores) from the surface materials and dust grains remain between grains. To assess the scattering behavior of the underlying basaltic granular medium, the area must be affected by stronger aeolian processes such as storms, to remove sufficiently dust both on the surface and within the substrate.

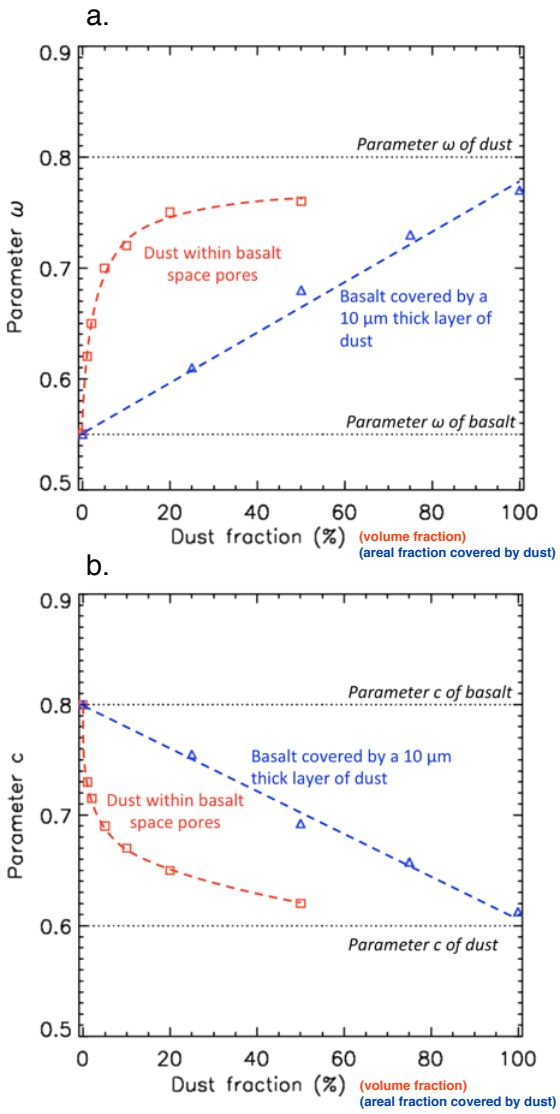

Figure 16: (Top) Evolution of the overall single scattering albedo (or parameter ω) and (Bottom) evolution of the overall backscattering fraction (or parameter c) of the mixture when adding dust (assumed as a clumping of small dust particles) to a soil made of basaltic granular medium. Both intimate (in red) and layered cases (in blue) are simulated. The grain sizes, optical parameters and phase functions used here are summarized in Table 3. For the intimate case, dust grains are set between the basaltic grains (Figure 14a). For the layered case, dust grains have a 10 microns size on top of the basaltic granular medium (Figures 14b and c). Since the porosity is set at 0.5, there are therefore always some voids between the dust grains.

Figure 17 represents the simulation for Meridiani Planum showing the simulation of the single scattering albedo (or parameter ω) (Figure 17a) and evolution of the backscattering fraction (parameter c) (Figure 17b), when adding hematite spheres (unique layer of spherules) on top of a basaltic granular medium. Figure 18 represents the evolution of the photometric curves, when adding hematite spheres on top of a soil made of fine grained sulfates. Hematite spheres are set randomly on top of the basaltic granular medium (Figure 15). Contrary to the case with a basaltic medium (Figure 17), geometric effects are very strong here, as demonstrated by *Pilorget et al.* (2015). As the hematite sphere areal density increases, the reflectance drops at high emission angles (the photons that come from the underlying sulfates encounter the hematite spheres and are absorbed when escaping with high emergence angles). This effect is very strong when bright materials partially covering with a very absorbent material. No satisfactory fit could be obtained when trying to mimic this photometric behavior but several trends can be observed as hematite spheres are added onto the surface : (i) the general reflectance factor level tends to drop, resulting in a decrease of the single scattering albedo, (ii) the reflectance factor tends to drop more strongly for high phase angles, which tends to limit forward scattering and develop a backscattering

behavior. Parameter ω drops from 0.98 (no hematite) to about 0.7 (40% hematite cover).

Results show that the addition of hematitic spherules to the basaltic medium or to the sulfate medium decreases the surface brightness (Figures 17a and 18) and increases the c values where the scattering became more backward (Figures 17b and 18). Similar results were observed by *Johnson et al.* (2013) where the additional of hematite-bearing spherules decreased the single scattering albedo (from 0.97 to 0.84 at 750 nm) and increased the backscattering fraction (from 0.16 to 0.419 at 750 nm).

By comparing the CRISM estimates for in the regions dominated by hematitic concretions on basaltic sands ($\omega_{CRISM} = 0.40 - 0.50$) to the simulations, results (Figure 17a) suggest that the basaltic layer on average may be covered by an areal fraction of hematite from 10 to 30%.

Moreover the modeling results suggest that regions where hematite-rich spherules cover the sulfate-rich deposits (Figure 7c, orange color unit), the spherules tend to control the overall photometric properties. By comparing the modeling results to the CRISM estimates, at least 40% of hematite spherules on top of the sulfate medium are needed to have similar CRISM single scattering albedo ($\omega_{CRISM} = 0.60 - 0.70$).

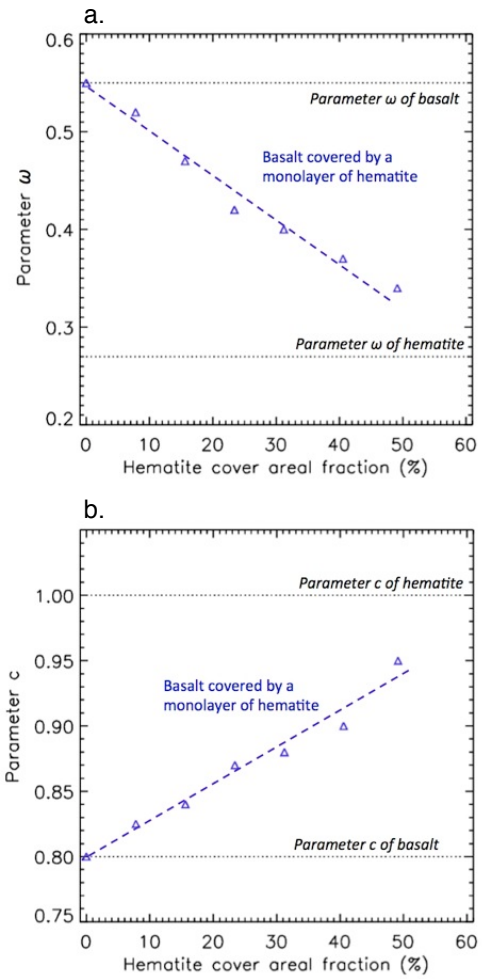

Figure 17: (Top) Evolution of the overall single scattering albedo (ω) and (Bottom) evolution of the overall backscattering fraction (c) of the mixture when adding hematite spheres (monolayer) on top of a soil made of basaltic sands. The grain sizes, optical parameters and phase functions used here are summarized in Table 3. Hematite spheres are set randomly on top of the basalic grains (Figure 15). The areal fraction covered by hematite spheres represents the surface occupied by the spheres when looking at nadir.

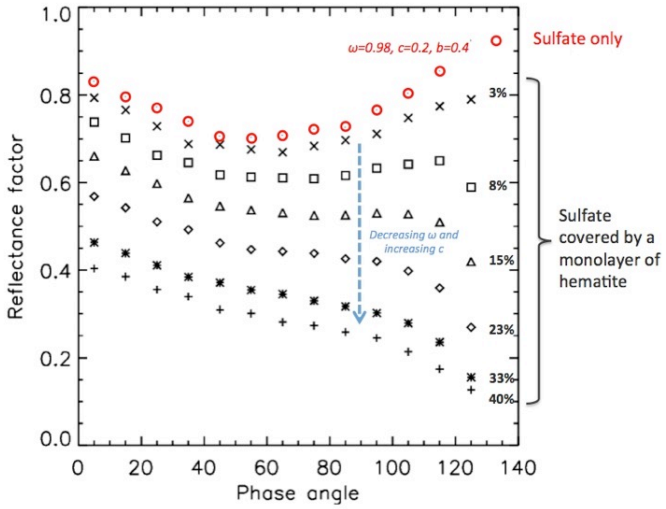

Figure 18: Evolution of the photometric curves when adding hematite spheres (monolayer) on top of a soil made of fine grained sulfates. The grain sizes, optical parameters and phase functions used here are summarized in Table 3. Hematite spheres are set randomly on top of the sulfate grains (Figure 15). The areal fraction covered by hematite spheres represents the surface occupied by the spheres when looking at nadir.

5 Relations to the geological processes

In the previous section, we underlined the main photometric results and tried to provide a physical meaning in terms of particle size, shape, internal structure and surface roughness. This section focuses on the identification and the characterization of geological processes from the surface photometric results.

5.1 Gusev Crater

Volcanic resurfacing with the formation of the primary basaltic crust The phase function parameters and the single scattering albedo values showed that the sand-sized basaltic granular medium (the dominating unit compared to the rocks in a CRISM pixel - 200 m/pxl) is composed of particles with moderate density internal scatterers. If the sand properties are similar to the properties of natural volcanic samples, then the sands may be characterized by internal structures such as micro-fractures, pores created by the escapement of gas during the magma crystallization, and/or crystals (microliths). The basaltic granular medium corresponds to the fractions of the basaltic rocks and crust which have been weathered. Due to the limitation of the spatial resolution of the MI instruments, the MI images cannot help us to understand the internal structure of the basaltic sands. However, the images of the basaltic rocks showed dark grey grains interpreted as olivine crystals (the biggest olivine crystals, larger than 100 μm representing up to 20-30 volume %) in an aphanitic groundmass (*McSween et al.*, 2006). The phenocrysts and more specifically the crystals and glass particles in the groundmass may act as internal scatterers which can explain the phase function parameters of the basaltic granular medium. This information provides key information about the magma crystallization phase.

Fragmentation of the volcanic crust by bolide impact The high macroscopic roughness values suggest the presence of a high population of angular ejecta materials (millimeter-sized scale) which are associated with the numerous craters, consistent with the presence of spaced clasts and rocks along the rover traverse (*Squyres et al.*, 2004a; *Grant et al.*, 2004, 2006; *Golombek et al.*, 2006; *Arvidson et al.*, 2006a; *Ward et al.*, 2005). This result reflects the fragmentation of the basaltic crust by local impacts and the emplacement of mm-sized ejecta materials in addition to the fragments resulting from typical physical weathering that comprise cm- and m-sized clasts and rocks.

Aeolian processes with the reworking of the unconsolidated materials The single scattering albedo values and the results presented in Section 4.1 indicate that dust seems to be a clumping of individual dust particles forming coarse aggregates. Consequently, the subparticles can act like internal scatterers. This observation suggests that coarser particles than the individual dust particle with 3 μm in diameter can be found. All these results are consistent with *Sullivan et al.* (2008); *Vaughan et al.* (2010)'s observations who identified the presence of dust aggregates ($\leq$150 μm) in local areas in

the MER-Spirit traverse, on the rover magnets and on solar panels. The aggregation of dust particles may be caused by electrostatic forces (*Greeley*, 1979). The aggregates are very fragile, porous and weakly dense which make them easier to be entrained by wind than individual dust particles or solid mafic grains of any large size ($\leq 300\mu m$) (*Sullivan et al.*, 2008; *Vaughan et al.*, 2010). Then, these aggregates disaggregate back into their $\leq 3\,\mu m$ particles by wind (*Sullivan et al.*, 2008) due to their fragility and the violence of the passing of dust devils or strong winds contributing dust to the atmosphere. The removal of dust by aeolian processes (storms and dust devils) exposes the lower-albedo basaltic media characterized by coarse grains. *Thomas et al.* (1984), *Edgett and Malin* (2000) and *Greeley et al.* (2005b) suggested that the removal of a few micrometers thickness of dust from the surface could create a reflectance difference as seen in the ω parameter map. This observation is also strengthened by the modeling results in Subsection 4.2 which showed that a dust cover can have a strong impact on the photometric response of the underlying basaltic medium. The phase function parameter values show that the basaltic sands are like rounded / spherical particles consistent with the in situ observations (*Greeley et al.*, 2006; *McGlynn et al.*, 2011). As discussed before, the Gusev basaltic crust was modified by bolide impacts. Consequently, the generated granular materials would be angular, such as typical lunar soils. The roundness of basaltic sands suggests that the materials were transported in long distance by wind and modified by post-aeolian processes (*McGlynn et al.*, 2011). In the regions affected by dust devil events, intermediate single scattering albedo values suggest that dust remains on the surface materials. The MI observations showed that dust infiltrates among the monolayer of basaltic sands which suggests these sands are not currently experiencing saltation (*Greeley et al.*, 2006). The radiative transfer modeling of an intimate mixture between dust and basaltic medium indicates that a small amount of dust can explain higher ω values and lower c values. Currently, only dust seems to be mobilized by aeolian processes (e.g., dust devils).

5.2 Meridiani Planum

Sulfate-rich deposits The ET2 unit is composed of sulfate-rich outcrops, identified in the aeolian ripple troughs and near the Endeavour crater rim. From HiRISE, the sulfate-rich outcrops in the ripple troughs are characterized by bright-toned materials whereas the sulfate-rich outcrops near the Endeavour crater are characterized by dark-toned materials. From photometric parameters, we noticed differences in the scattering behaviors between both etched terrains:

(1) The dark-toned etched terrains have lower ω than the bright-toned terrains ($\omega = 0.40 - 0.50$ for dark-toned etched terrains, $\omega = 0.60 - 0.65$ for bright-toned etched terrains). This result can be explained by the presence of coarser-grained particles in the dark-toned etched terrains.

(2) The dark-toned and bright-toned etched terrains have high c ($c > 0.75$ for dark-toned etched terrains, $c < 0.75$ for bright-toned etched terrains). This suggests the presence of a heterogenous internal structures (even the first microns) created by mixtures of sulfates and very fine-grained siliciclastic materials, crystalline textures of subsequently precipitated cements and areas of recrystallization, centimeter-size vugs that record the early diagenetic growth and subsequent dissolution of crystals, and millimeter in size of spherules embedded in the outcrops (*Herkenhoff et al.*, 2004b, 2008). The internal heterogeneity may suggest a complex history of their formation, more especially during the precipitation and diagenesis phases. These phases may be composed of subsequent events of local recrystallization of cements and dissolution of the mineral grains and their evolution due to direct exposure and desiccation (*Squyres et al.*, 2004c). Moreover, higher values of parameter c are noticed for the dark-toned etched outcrops which may be explained by the presence of a greater heterogeneity.

(3) The dark-toned etched terrains have lower $\bar{\theta}$ than the bright-toned terrains ($\bar{\theta}$ =5° for dark-toned etched terrains, $\bar{\theta}$ =15-25° for bright-toned etched terrains). This result can be explained by the presence of flat sedimentary rocks, and/or less desiccated rocks in the dark-toned regions.

The modeling results presented in Section 4.2 suggested that regions where hematite-rich spherules cover the bright sulfate-rich deposits tends to control the overall photometric properties, masking the photometric behavior of the underlying materials.

Lag of hematitic concretions The Pm unit is characterized by a mixture of hematitic concretions on basaltic sands. The single scattering albedo values and the phase function parameter values underlined the presence of coarse spherical hematitic concretions with moderate density of internal structure.

6 Conclusion

CRISM multi-angular observations allow for the characterization of the surface scattering behavior, which depends on the composition but also the material physical properties, such as the grain size and distribution, shape, internal structure, and the surface roughness and porosity. First an atmospheric correction (compensating mineral aerosol effects) by the MARS-ReCO algorithm was used to estimate more accurately the surface photometric curve taking into account the

surface and mineral aerosol scattering anisotropy. Then the surface photometric curve was analyzed by inverting the Hapke photometric model depending on six parameters: single scattering albedo, 2 phase function terms, macroscopic roughness and 2 opposition effects terms, in a Bayesian framework. Surface photometric maps were created to observe the spatial variations of surface scattering properties at the CRISM spatial resolution (∼200m/pixel), as a function of geological units. The orbital observations of the MER landing site regions in Gusev Crater and Meridiani Planum were used for interpreting the estimated Hapke photometric parameters in terms of physical properties, which can provide useful information about the geological processes. The in situ observations were used as ground truth to validate the interpretations.

Variable scattering properties were observed within a CRISM observation (∼5x10km) as a function of geological units suggesting variations of surface physical properties. Such variations suggest that surfaces are controlled by local geological processes rather than regional or global processes, like volcanic resurfacing, fragmentation by impacts, aeolian processes, sulfates deposition and diagenesis.

Results are consistent with the in situ observations, thus validating the approach and the use of photometry for the estimates of Martian surface physical properties. Some discrepancies resulted from a difference in the spatial scales. From the ground, the in situ instruments can distinguish rocks and soils (centimeter spatial scale), whereas CRISM observes extended areas (hectometric spatial scale) composed of different components of the surface (rocks and soils).

Future works will focus on the determination of surface photometric parameters of different geological terrains (sedimentary, volcanic terrains, impact craters, etc), in order to identify variabilities of scattering properties on Mars.

Appendix A: Calculation of the single scattering albedo from *Hapke* (2012a)'s formulation

The single scattering albedo, ω, is the ratio of scattered light at the particle scale to extincted light and depends on the complex indices of refraction (n and k) related to the particle composition, the path length ($< D >$) related to the particle size, the internal scattering coefficient (s) and the density of internal scatterers (sD) related to the particle internal structure. The single scattering albedo varies from 0 (the light is totally absorbed) to 1 (the light is totally scattered) and it is defined as follows by *Hapke* (2012b):

$$\omega = \frac{Q_S}{Q_E} = \frac{Q_S}{Q_S + Q_A} \tag{1}$$

where Q_S is the scattering efficiency of a particle and Q_E the extinction efficiency of a particle

In the case of particles larger than the wavelength in a dense granular medium, the diffraction is ignored, so $Q_E = 1$ (*Hapke*, 2012a) and then:

$$\omega = Q_S \tag{2}$$

The scattering efficiency (nondiffractive) of large particles is the sum of two effiencies: (1) the total fraction of incident light that is reflected or emerges from the back surface of the slab (the surface facing the source) referred to as the backscattering efficiency, and (2) that emerging from the forward surface of the slab (the surface facing away from the source), referred to as the forward-scattering efficiency. *Hapke* (2012a) (Eq. 6.20) provided the following equation for Q_S:

$$Q_S = S_E + \frac{(1 - S_E)\,(1 - S_I)}{1 - S_I\,\Theta}\,\Theta \tag{3}$$

- S_E is the surface reflection coefficient for light that is externally incident on an irregular particle. *Hapke* (2012a) (Eq. 6.49a) provided an analytic approximation to S_E given by:

$$S_E = 0.0587 + 0.8543\,R(0) + 0.0870\,R(0)^2 \tag{4}$$

  with $R(0)$, the normal specular reflection coefficient (*Hapke*, 2012a) (Eq. 6.49a): $R(0) = \frac{(n-1)^2+k^2}{(n+1)^2+k^2}$

- S_I is the surface reflection coefficient for light that is internally incident on a particle. An approximation to S_I is given by *Hapke* (2012a) (Eq. 6.23) as follows:

$$S_I = 1 - \frac{1}{n^2}\,(0.9413 - 0.8543\,R(0) - 0.08710\,R(0)^2) \tag{5}$$

- Θ is the internal-transmission factor and the expression is (*Hapke*, 2012a) (Eq. 6.30):

$$\Theta = \frac{r_i + exp(-\sqrt{(\alpha \times (\alpha + s)} < D >)}{1. + r_i \, exp(-\sqrt{(\alpha \times (\alpha + s)} < D >)} \tag{6}$$

  with r_I, the internal diffusive reflectance (*Hapke*, 2012a) (Eq. 6.48b): $r_I = \frac{1-\sqrt{\alpha/(\alpha+s)}}{1+\sqrt{\alpha/(\alpha+s)}}$

  with α, the absorption coefficient: $\alpha = \frac{4\pi k}{\lambda}$

- s is the internal scattering coefficient, expressed in length^{-1}. If $s = 0$, that means that there are no internal scatterers inside the particle. The s parameter describes the light attenuation by scattering caused by the presence of internal scatterers (*Hapke*, 2012a).

- $< D >$ is the mean ray path length through particle in the case where there are no internal scatterers. If the particle is spherical then $< D >= 0.9 \times D$ where D is the mean diameter of the particle. If the particle is irregular, $< D >$ could be quite different from D (in general will be smaller) (*Hapke*, 2012a).

Acknowledgement This work was supported by the French Space Agency CNES (Centre National d'Etudes Spatiales) and PNP (Programme National de Planétologie) from INSU (Institut National des Sciences de l'Univers). The authors would like to thank Michael Wolff for making his aerosol optical thickness values available for this study, the CRISM team for providing the data. Finally, we would like to gratefully thank Jeffrey Johnson and the anonymous reviewer for their constructive comments which substantially improved the manuscript.

References

Arvidson, R. E., et al. (2006a), Overview of the Spirit Mars Exploration Rover mission to Gusev Crater: Landing site to Backstay Rock in the Columbia Hills, *J. Geophys. Res.*, *111*, E02S01, doi:10.1029/2005JE002499.

Arvidson, R. E., et al. (2006b), Nature and origin of the hematite-bearing plains of Terra Meridiani based on analyses of orbital and Mars Exploration rover data sets, *J. Geophys. Res.*, *111*, E12S08, doi:10.1029/2006JE002728.

Arvidson, R. E., et al. (2008), Spirit Mars Rover Mission to the Columbia Hills, Gusev Crater: Mission overview and selected results from the Cumberland Ridge to Home Plate, *Journal of Geophysical Research: Planets*, *113*(E12), n/a–n/a, doi:10.1029/2008JE003183.

Arvidson, R. E., et al. (2011), Opportunity Mars Rover mission: Overview and selected results from Purgatory ripple to traverses to Endeavour crater, *Journal of Geophysical Research: Planets*, *116*(E7), n/a–n/a, doi:10.1029/2010JE003746.

Arvidson, R. E., et al. (2014), Ancient Aqueous Environments at Endeavour Crater, Mars, *Science*, *343*(6169), n/a–n/a, doi:10.1126/science.1248097.

Bandfield, J. L., and C. S. Edwards (2008), Derivation of martian surface slope characteristics from directional thermal infrared radiometry, *Icarus*, *193*(1), 139 – 157, doi:http://dx.doi.org/10.1016/j.icarus.2007.08.028.

Bell, J. F., et al. (2004), Pancam Multispectral imaging Results from the Spirit Rover at Gusev Crater, *Science*, *305, no. 5685*, 800–806, doi:10.1126/science.1100175.

Cabrol, N. A., et al. (2003), Exploring Gusev Crater with Spirit: Review of science objectives and testable hypotheses, *Journal of Geophysical Research: Planets*, *108*(E12), n/a–n/a, doi:10.1029/2002JE002026.

Campbell, B. A. (2001), Radar backscatter from Mars: Properties of rock-strewn surfaces, *Icarus*, *150*(1), 38 – 47, doi:http://dx.doi.org/10.1006/icar.2000.6566.

Ceamanos, X., S. Douté, J. Fernando, F. Schmidt, P. Pinet, and A. Lyapustin (2013), Surface reflectance of Mars observed by CRISM/MRO: 1. Multi-angle Approach for Retrieval of Surface Reflectance from CRISM Observations (MARS-ReCO), *J. Geophys. Res.*, *118*, doi:10.1029/2012JE004195.

Chojnacki, M., J. Moerch, J. Wray, and D. Burr (2010), The stratigraphy, composition and thermophysical properties of Endeavour crater, Meridiani Planum, Mars, from orbital remote sensing, *Lunar Planet. Sci.*, *XXXXI*, abstract 2175.

Christensen, P. R., et al. (2000), Detection of crystalline hematite mineralization on Mars by the Thermal Emission Spectrometer: Evidence for near-surface water, *J. Geophys. Res.*, *115*, 9623–9642, doi:10.1029/1999JE001093.

Christensen, P. R., R. V. Morris, M. D. Lane, J. L. Bandfield, and M. C. Malin (2001), Global mapping of Martian hematite mineral deposits: Remnants of water-driven processes on early Mars, *Journal of Geophysical Research: Planets*, *106*(E10), 23,873–23,885, doi:10.1029/2000JE001415.

Christensen, P. R., et al. (2004), Initial results from the Mini-TES experiment in Gusev c-Crater from the spirit rover, *Science*, *305, 5685*, 837–842, doi:10.1126/science.1100564.

Cord, A. M., P. C. Pinet, Y. Daydou, and S. D. Chevrel (2003), Planetary regolith surface analogs: Optimized determination of Hapke parameters using multi-angular spectro-imaging laboratory data, *Icarus*, *165*, 414–427, doi:10.1016/S0019-1035(03)00204-5.

Cord, A. M., P. C. Pinet, Y. Daydou, and S. D. Chevrel (2005), Experimental determination of the surface photometric contribution in the spectral reflectance deconvolution processes for a simulated martian crater-like regolithic target, *Icarus*, *175*, 78–91, doi:10.1016/j.icarus.2004.08.010.

Edgett, K. S., and M. C. Malin (2000), Martian dust raising and surface albedo controls: Thin, dark (and sometimes bright) streaks and dust devils in MGS MOC high resolution images, *Lunar Planet. Sci.*, *XXXI*, abstract 1073.

Erard, S., J. Mustard, S. Murchie, J. P. Bibring, P. Cerroni, and A. Coradini (1994), Martian aerosols: Near-infrared spectral properties and effects on the observation of the surface, *Icarus*, *111*, 317–337, doi:10.1006/icar.1994.1148.

Fernando, J., F. Schmidt, X. Ceamanos, P. Pinet, S. Douté, and Y. Daydou (2013a), Surface reflectance of Mars observed by CRISM/MRO: 2. Estimation of surface photometric properties in Gusev Crater and Meridiani Planum, *J. Geophys. Res.*, *118*, doi:10.1029/2012JE004194.

Fernando, J., F. Schmidt, X. Ceamanos, P. Pinet, S. Douté, and Y. Daydou (2013b), Estimation of surface photometric parameters: Bayesian inversion on Hapke's model, *EPSC*, *Vol. 8*, abstract 574.

Glotch, T. D., R. V. Morris, P. R. Christensen, and T. G. Sharp (2004), Effect of precursor mineralogy on the thermal infrared emission spectra of hematite: Application to Martian hematite mineralization, *Journal of Geophysical Research: Planets*, *109*(E7), n/a–n/a, doi:10.1029/2003JE002224.

Glotch, T. D., P. R. Christensen, and T. G. Sharp (2006), Fresnel modeling of hematite crystal surfaces and application toMartian hematite spherules, *Icarus*, *181*(2), 408 – 418, doi:http://dx.doi.org/10.1016/j.icarus.2005.11.020.

Golden, D. C., D. W. Ming, R. V. Morris, and T. G. Graff (2008), Hydrothermal synthesis of hematite spherules and jarosite: Implications for diagenesis and hematite spherule formation in sulfate outcrops at Meridiani Planum, Mars, *American Mineralogist*, *93*, 1201–1214, doi:10.2138/am.2008.2737.

Golden, D. C., D. W. Ming, and R. V. Morris (2010), Spherulitic growth of hematite under hydrothermal conditions: Insights into the growth mechanism of hematite spherules at Meridiani Planum, Mars, *Lunar Planet. Sci.*, *abstract 2541*.

Golombek, M. P., et al. (2006), Geology of the Gusev cratered plains from the Spirit rover transverse, *J. Geophys. Res.*, *111*, E02S07, doi:10.1029/2005JE002503.

Grant, J. A., et al. (2004), Surficial deposits at Gusev Crater along Spirit rover traverses, *Science*, *305*, no. 5685, doi:10.1126/science.1099849.

Grant, J. A., S. A. Wilson, M. Ruff, S. W. Golombek, and D. Koestler (2006), Distribution of roacks on the Gusev plains and on Husband Hill, Mars, *J. Geophys. Res.*, *33*, L16,202, doi:10.1029/2006GL026964.

Greeley, R. (1979), Silt-clay aggregates on Mars, *Journal of Geophysical Research: Solid Earth*, *84*(B11), 6248–6254, doi:10.1029/JB084iB11p06248.

Greeley, R., et al. (1993), Galileo imaging observations of Lunar maria and related deposits, *Journal of Geophysical Research: Planets*, *98*(E9), 17,183–17,205, doi:10.1029/93JE01000.

Greeley, R., R. O. Kuzmin, S. C. R. Rafkin, T. I. Michaels, and R. Haberle (2003), Wind-related features in Gusev Cater, Mars, *J. Geophys. Res.*, *108*, E128,077, doi:10.1029/2002JE002006.

Greeley, R., et al. (2004), Wind-related processes detected by the Spirit rover at Gusev Crater, Mars, *Science*, *305*, no. 5685, doi:10.1126/science.1100108.

Greeley, R., B. H. Foing, H. Y. M. Jr., G. Neukum, M. v. K. P. Pinet, S. C. Werner, D. A. Williams, and T. E. Zegers (2005a), Fluid lava flows in Gusev Crater, Mars, *J. Geophys. Res.*, *110*, E05,008, doi:10.1029/2005JE002401.

Greeley, R., et al. (2005b), Martian variable features: New insight from the Mars Express orbiter and the Mars Exploration Rover Spirit, *J. Geophys. Res.*, *110*, E06,002, doi:10.1029/2005JE002403.

Greeley, R., et al. (2006), Gusev Crater: Wind-related features and processes observed by the Mars Exploration Rover Spirit, *J. Geophys. Res.*, *111*, E02S09, doi:10.1029/2005JE002491.

Grotzinger, J., et al. (2005), Stratigraphy and sedimentology of a dry to wet eolian depositional system, burns formation, Meridiani Planum, Mars, *Earth and Planetary Science Letters*, *240*(1), 11 – 72, doi:http://dx.doi.org/10.1016/j.epsl.2005.09.039, <ce:title>Sedimentary Geology at Meridiani Planum, Mars</ce:title>.

Hapke, B. (1993), *Theory of Reflectance and Emittance Spectroscopy*, Cambridge Univ. Press.

Hapke, B. (2012a), *Theory of Reflectance and Emittance Spectroscopy*, Cambridge Univ. Press.

Hapke, B. (2012b), Bidirectional reflectance spectroscopy 7 the single particle phase function hocky stick relation, *Icarus*, *221*, 1079–1083, doi:10.1016/j.icarus.2012.10.022.

Helfenstein, P. (1988), The geological interpretation of photometric surface roughness, *Icarus*, *73*, 462–481, doi:10.1016/0019-1035(88)90056-5.

Helfenstein, P., and M. K. Shepard (1999), Submillimeter-scale topography of the Lunar regolith, *Icarus*, *141*(1), 107 – 131, doi:http://dx.doi.org/10.1006/icar.1999.6160.

Herkenhoff, K. E., et al. (2004a), Textures of the soils and rocks at Gusev Crater from Spirit's Microscopic Imager, *Science*, *305*, 5685, doi:10.1126/science.3050824.

Herkenhoff, K. E., et al. (2004b), Evidence from Opportunity's Microscopic Imager for water on Meridiani Planum, *Science*, *306*(5702), 1727–1730, doi:10.1126/science.1105286.

Herkenhoff, K. E., et al. (2008), Surface processes recorded by rocks and soils on Meridiani Planum, Mars: Microscopic Imager observations during Opportunity's first three extended missions, *J. Geophys. Res.*, *113*, E12S32, doi:10.1029/2008JE003100.

Herkenhoff, K. E., et al. (2006), Overview of the Microscopic Imager investigation during Spirit's first 450 sols in Gusev Crater, *J. Geophys. Res.*, *111*, E02S04, doi:10.1029/2005JE002574.

Jehl, A., et al. (2008), Gusev photometric variability as seen from orbit by HRSC/Mars-Express, *Icarus*, *197*, 403–428, doi:10.1016/j.icarus.2008.05.022.

Jerolmack, D. J., D. Mohrig, J. P. Grotzinger, D. A. Fike, and W. A. Watters (2006), Spatial grain size sorting in eolian ripples and estimation of wind conditions on planetary surfaces: Application to Meridiani Planum, Mars, *J. Geophys. Res.*, *111*, E12S02, doi:10.1029/2005JE002544.

Johnson, J. R., et al. (1999), Preliminary results on photometric properties of materials at the Sagan Memorial Station, Mars, *J. Geophys. Res.*, *104*, 8809–8830, doi:doi:10.1029/98JE02247.

Johnson, J. R., et al. (2006a), Spectrophotometric properties of materials observed by Pancam on the Mars Exploration Rovers: 1. Spirit, *J. Geophys. Res.*, *111*, E02S14, doi:10.1029/2005JE002494.

Johnson, J. R., et al. (2006b), Spectrophotometric properties of materials observed by Pancam on the Mars Exploration Rovers: 2. Opportunity, *J. Geophys. Res.*, *111*, E12S16, doi:10.1029/2006JE002762.

Johnson, J. R., et al. (2006c), Radiative transfer modeling of dust-coated pancam calibration target materials: Laboratory visible/near-infrared spectrogoniometry, *J. Geophys. Res.*, *111*, E12S07, doi:10.1029/2005JE002658.

Johnson, J. R., M. K. Shepard, W. Grundy, D. A. Paige, and E. Foote (2013), Spectrometry and modeling of Martian and Lunar analog samples and Apollo soils, *Icarus*, *223*, 383–406, doi:10.1016/j.icarus.2012.12.004.

Johnson, J. R., W. Grundy, M. T. Lemmon, J. F. Bell III, and R. G Deen (2014), Spectrophotometric properties of materials observed by Pancam on the Mars Exploration Rovers: 3. Sols 500-1525, *Icarus*, *248*, 27–71, doi:10.1016/j.icarus.2014.10.026.

Kuzmin, R., R. Greeley, R. Landheim, N. Cabrol, and J. Farmer (2000), Geologic map of the MTM-15182 and MTM-15187 quadrangles, Gusev crater Ma'adim Vallis region, *Mars. Geologic Investigative Series, U.S. Geological Survey, Reston, VA*.

Lane, M. D., R. V. Morris, S. A. Mertzman, and P. R. Christensen (2002), Evidence for platy hematite grains in Sinus Meridiani, Mars, *Journal of Geophysical Research: Planets*, *107*(E12), 9–1–9–15, doi:10.1029/2001JE001832.

Lemmon, M. T., et al. (2004), Atmospheric imaging results from the Mars Exploration Rovers: Spirit and Opportunity, *Science*, *306*, doi:10.1126/science.1104474.

Lichtenberg, K. A., et al. (2007), Coordinated analyses of orbital and Spirit rover data to characterize surface materials on the cratered plains of Gusev Crater, Mars, *J. Geophys. Res.*, *112*, E12S90, doi:10.1029/2006JE002850.

Lucey, P. (1998), Model near-infrared optical constants of olivine and pyroxene as a function of iron content, *J. Geophys. Res. 103*, 1703–1713, doi:10.1029/97JE03145.

Martinez-Alonso, S., B. M. Jakosky, M. T. Mellon, and N. E. Putzig (2005), A volcanic interpretation of Gusev Crater surface materials from thermophysical, spectral, and morphological evidence, *J. Geophys. Res.*, *110*, E01,003, doi:10.1029/2004JE002327.

McGlynn, I. O., C. M. Fedo, and H. Y. McSween (2011), Origin of basaltic soils at Gusev Crater, Mars, by aeolian modification of impact-generated sediment, *J. Geophys. Res.*, *116*, E00F22, doi:10.1029/2010JE003712.

McGuire, A., and B. Hapke (1995), An experimental study of light scattering by large irregular particles, *Icarus*, *113*, 134–155, doi:10.1006/icar.1995.1012.

McLennan, S., et al. (2005), Provenance and diagenesis of the evaporite-bearing Burns formation, Meridiani Planum, Mars, *Earth and Planetary Science Letters*, *240*(1), 95 – 121, doi:http://dx.doi.org/10.1016/j.epsl.2005.09.041, <ce:title>Sedimentary Geology at Meridiani Planum, Mars</ce:title>.

McSween, H. Y. et al. (2004), Basaltic rocks analyzed by the spirit rover in Gusev Crater, *Science*, *305*, 5685, doi:10.1126/science.3050842.

McSween, H. Y., et al. (2006), Characterization and petrologic interpretation of olivine-rich basalts at Gusev Crater, Mars, *Journal of Geophysical Research: Planets*, *111*(E2), n/a–n/a, doi:10.1029/2005JE002477.

Milam, K. A., K. R. Stockstill, J. E. Moersch, J. McSween, Harry Y., L. L. Tornabene, A. Ghosh, M. B. Wyatt, and P. R. Christensen (2003), THEMIS characterization of the MER Gusev Crater landing site, *J. Geophys. Res.*, *108*, E12,8078, doi:10.1029/2002JE002023.

Mosegaard, K., and A. Tarantola (1995), Monte Carlo sampling of solutions to inverse problems, *J. Geophys. Res.*, *100*, 12,431–12,447, doi:10.1029/94JB03097.

Murchie, S. (2012), CRISM on MRO - instrument and investigation overview, *in MRO/CRISM Data Users' Workshop, The Woodlands, TX*.

Murchie, S. et al. (2007), Compact Reconnaissance Imaging Spectrometer for Mars (CRISM) on Mars Reconnaissance Orbiter MRO, *J. Geophys. Res.*, *112*, E05S03, doi:10.1029/2006JE002682.

Neumann, G. A., J. B. Abshire, O. Aharonson, J. B. Garvin, X. Sun, and M. T. Zuber (2003), Mars Orbiter Laser Altimeter pulse width measurements and footprint-scale roughness, *Geophys. Res. Lett.*, *30*, doi:10.1029/2002JE001849.

Piatek, J., B. Hapke, R. Nelson, W. Smythe, and A. Hale (2004), Scattering properties of planetary regolith analogs, *Icarus*, *171*, 531–545, doi:10.1016/j.icarus.2004.05.019.

Pilorget, C., M. Vincendon, and F. Poulet (2013), A radiative transfer model to simulate light scattering in a compact granular medium using a Monte-Carlo approach: Validation and first applications, *Journal of Geophysical Research: Planets*, doi:10.1002/2013JE004465.

Pilorget, C., J. Fernando, B. L. Ehlmann, and S. Douté (2015), Photometry of particulate mixtures: what controls the phase curve?, *Icarus*, *250*, pp. 188 – 203, doi:10.1016/j.icarus.2014.11.036.

Pinet, P. C., et al. (2005), Derivation of Mars surface scattering properties from OMEGA spot pointing, *Lunar Planet. Sci.*, *XXXVI*, abstract 1694.

Pollack, J. B., O. B. Toon, and B. N. Khare (1973), Optical properties of some terrestrial rocks and glasses, *Icarus*, *19*(3), 372 – 389, doi:http://dx.doi.org/10.1016/0019-1035(73)90115-2.

Pommerol, A., N. Thomas, B. Jost, P. Beck, C. Okubo, and A. McEwen (2013), Photometric properties of Mars soils analogs, *J. Geophys. Res.*

Poulet, F., C. Gomez, J.-P. Bibring, Y. Lanagan, B. Gondet, P. Pinet, and J. Belluci, G. Mustard (2007), Martian surface mineralogy from Observation pour la Mineralogie, l'Eau, les Glaces et l'Activite on board the Mars Express spacecraft (OMEGA/MEx): Global mineral maps, *J. Geosphys. Res.*, *112*, E08S02, doi:10.1029/2006JE002840.

Roush, T. L., F. Esposito, G. R. Rossman, and L. Colangeli (2007), Estimated optical constants of gypsum in the regions of weak absorptions: Application of scattering theories and comparisons to independent measurements, *Journal of Geophysical Research: Planets*, *112*(E10), n/a–n/a, doi:10.1029/2007JE002920.

Shaw, A., M. J. Wolff, F. P. Seelos, S. M. Wiseman, and S. Cull (2013), Surface scattering properties at the Opportunity mars rover's traverse region measured by CRISM, *Journal of Geophysical Research: Planets*, *118*(8), 1699–1717, doi: 10.1002/jgre.20119.

Shepard, M. K., and B. A. Campbell (1998), Shadows on a planetary surface and implications for photometric roughness, *Icarus*, *134*, 279–291.

Shepard, M. K., and P. Helfenstein (2007), A test of the Hapke photometric model, *J. Geophys. Res.*, *112*, E03,001, doi:10.1029/2005JE002625.

Shkuratov, Y. G., D. G. Stankevich, D. V. Petrov, P. C. Pinet, A. M. Cord, Y. H. Daydou, and S. D. Chevrel (2005), Interpreting photometry of regolith-like surfaces with different topographies, *Icarus*, *173*, doi:10.1016/j.icarus.2003.12.017.

Soderblom, L. A., et al. (2004), Soils of Eagle Crater and Meridiani Planum at the Opportunity rover landing site, *Science*, *306*, 1723, doi:10.1126/science.1105127.

Sokolik, I. N., and O. B. Toon (1999), Incorporation of mineralogical composition into models of the radiative properties of mineral aerosol from UV to IR wavelengths, *Journal of Geophysical Research: Atmospheres*, *104*(D8), 9423–9444, doi:10.1029/1998JD200048.

Souchon, A. L., P. Pinet, S. Chevrel, Y. Daydou, D. Baratoux, K. Kurita, M. K. Shepard, and P. Helfenstein (2011), An experimental study of Hapke's modeling of natural granular surface samples, *Icarus*, *215*, 313–331, doi:10.1016/j.icarus.2011.06.023.

Squyres, S. W., et al. (2004a), The Spirit rover's Athena Science Investigation at Gusev Crater, Mars, *Science*, *305*, 794, doi:10.1126/science.3050794.

Squyres, S. W., et al. (2004b), The Opportunity rover's Athena Science Investigation at Meridiani Planum, Mars, *Science*, *306*, 1698, doi:10.1126/science.1106171.

Squyres, S. W., et al. (2004c), In situ evidence for an ancient aqueous environment at Meridiani Planum, Mars, *Science*, *306*(5702), 1709–1714, doi:10.1126/science.1104559.

Squyres, S. W., et al. (2006), Overview of the Opportunity Mars Exploration Rover mission to Meridiani Planum: Eagle Crater to Purgatory Ripple, *J. Geophys. Res.*, *111*, E12S12, doi:10.1029/2006JE002771.

Squyres, S. W. et al. (2006), Two years at Meridiani Planum: Results from the Opportunity rover, *Science*, *313*, 1403, doi:10.1126/science.1130890.

Sullivan, R., et al. (2005), Aeolian processes at the Mars Exploration Rover Meridiani Planum landing site, *Nature*, *436*, 58–61, doi:10.1038/nature03641.

Sullivan, R., et al. (2008), Wind-driven particle mobility on Mars: Insights from Mars Exploration Rover observations at "El Dorado" and surroundings at Gusev Crater, *Journal of Geophysical Research: Planets*, *113*(E6), doi:10.1029/2008JE003101.

Tarantola, A., and B. Valette (1982), Inverse problems=quest for information, *J. Geophys*, *50*, 159–170.

Thomas, P., J. Veverka, D. Gineris, and L. Wong (1984), "dust" streaks on Mars, *Icarus*, *58*, 331–338.

Tomasko, M. G., L. R. Doose, M. Lemmon, P. H. Smith, and E. Wegryn (1999), Properties of dust in the Martian atmosphere from the imager on Mars Pathfinder, *Journal of Geophysical Research: Planets*, *104*(E4), 8987–9007, doi:10.1029/1998JE900016.

Vaughan, A., J. Johnson, K. E. Herkenhoff, R. Sullivan, G. A. Landis, W. Goetz, and M. B. Madsen (2010), Pancam and Microscopic Imager observations of dust on the Spirit rover: Cleaning events, spectral properties, and aggregates, *Mars 5*, pp. 129–145.

Ward, J. G., R. E. Arvidson, and M. Golombek (2005), The size-frequency and areal distribution of rock clasts at the Spirit landing site, Gusev Crater, mars, *Geophys. Res. Lett.*, *32*, L11,203, doi:10.1029/2005GL022705.

Weitz, C. M., et al. (2006), Soil grain analyses at Meridiani Planum, Mars, *J. Geosphys. Res.*, *111*, E12S04, doi:10.1029/2005JE002541.

Wolff, M. J., M. D. Smith, R. T. Clancy, R. Arvidson, M. Kahre, F. Seelos, S. Murchie, and H. Savijarvi (2009), Wavelength dependance of dust aerosol single scaterring albedo as observed by the Compact Reconnaissance Imaging Spectrometer, *J. Geophys. Res.*, *114*, E00D64, doi:doi:10.1029/2009JE003350.

Wray, J. J., E. Z. Noe Dobrea, R. E. Arvidson, S. M. Wiseman, S. W. Squyres, A. S. McEwen, J. F. Mustard, and S. L. Murchie (2009), Phyllosilicates and sulfates at Endeavour Crater, Meridiani Planum, Mars, *Geophysical Research Letters*, *36*(21), n/a–n/a, doi:10.1029/2009GL040734.